



**HAL**  
open science

## Forebrain Eml1 depletion reveals early centrosomal dysfunction causing subcortical heterotopia

Donia Zaidi, Kaviya Chinnappa, Berfu Nur Yigit, Valeria Viola, Carmen Cifuentes-Diaz, Ammar Jabali, Ana Uzquiano, Emilie Lemesre, Franck Perez, Julia Ladewig, et al.

### ► To cite this version:

Donia Zaidi, Kaviya Chinnappa, Berfu Nur Yigit, Valeria Viola, Carmen Cifuentes-Diaz, et al.. Forebrain Eml1 depletion reveals early centrosomal dysfunction causing subcortical heterotopia. *Journal of Cell Biology*, 2024, 223 (12), 10.1083/jcb.202310157 . hal-04721394

**HAL Id: hal-04721394**

<https://hal.sorbonne-universite.fr/hal-04721394v1>

Submitted on 4 Oct 2024

**HAL** is a multi-disciplinary open access archive for the deposit and dissemination of scientific research documents, whether they are published or not. The documents may come from teaching and research institutions in France or abroad, or from public or private research centers.

L'archive ouverte pluridisciplinaire **HAL**, est destinée au dépôt et à la diffusion de documents scientifiques de niveau recherche, publiés ou non, émanant des établissements d'enseignement et de recherche français ou étrangers, des laboratoires publics ou privés.

# 1           **Forebrain Eml1 depletion reveals early centrosomal** 2           **dysfunction causing subcortical heterotopia**

3           Donia Zaidi<sup>1,2,3</sup>; Kaviya Chinnappa<sup>1,2,3</sup>; Berfu Nur Yigit<sup>4</sup>; Valeria Viola<sup>1,2,3</sup>;  
4           Carmen Cifuentes-Diaz<sup>1,2,3</sup>; Ammar Jabali<sup>5,6,7</sup>; Ana Uzquiano<sup>8,9</sup>; Emilie Lemesre<sup>10</sup>; Franck  
5           Perez<sup>10</sup>; Julia Ladewig<sup>5,6,7</sup>; Julien Ferent<sup>1,2,3</sup>; Nurhan Ozlu<sup>4,11</sup>; Fiona Francis<sup>1,2,3</sup>#

6           1 : Institut du Fer à Moulin, 75005 Paris, France.

7           2 : Institut National de Santé et de Recherche Médicale (INSERM, UMR-S 1270), Paris,  
8           France.

9           3: Sorbonne Université, Paris, France.

10          4: Koc University, Department of Molecular Biology and Genetics, İstanbul, Turkiye,

11          5: Central Institute of Mental Health (ZI), Medical Faculty Mannheim, Heidelberg University,  
12          Mannheim Germany.

13          6: Hector Institute for Translational Brain Research (HITBR), Mannheim, Germany.

14          7: German Cancer Research Center (DKFZ), Heidelberg, Germany.

15          8: Harvard University, Department of Stem Cell and Regenerative Biology, Cambridge, AL,  
16          United States of America.

17          9: Stanley Center for Psychiatric Research, Broad Institute of MIT and Harvard, Cambridge,  
18          AL, United States of America.

19          10: Dynamics of Intracellular Organization Laboratory, Institut Curie, PSL Research  
20          University, Sorbonne Université, Centre National de la Recherche Scientifique, UMR 144,  
21          Paris, France.

22          11: Koc University, Research Center for Translational Medicine (KUTTAM), İstanbul,  
23          Turkiye.

24          # Corresponding author : Fiona Francis, Institut du Fer à Moulin, 17 rue du Fer à Moulin,  
25          75005 Paris, France. Tel: +33145876142 Email: fiona.francis@inserm.fr

## 26          **eTOC summary**

27          Mechanisms leading to abnormal distribution of neural progenitors during cortical  
28          development in the context of subcortical heterotopia associated with EML1 mutations remain  
29          unknown. Using a forebrain-specific mouse model and mutant human cells, this work  
30          innovatively demonstrates that by restoring microtubule function, abnormal progenitor  
31          distribution and heterotopic volume are significantly reduced.



## 33 **Abstract**

34 Subcortical heterotopia is a cortical malformation associated with epilepsy, intellectual  
35 disability and an excessive number of cortical neurons in the white matter. EML1  
36 (Echinoderm microtubule associated protein like 1) mutations lead to subcortical heterotopia,  
37 associated with abnormal radial glia positioning in the cortical wall, prior to malformation  
38 onset. This perturbed distribution of proliferative cells is likely to be a critical event for  
39 heterotopia formation, however the underlying mechanisms remain unexplained. This study  
40 aimed to decipher the early cellular alterations leading to abnormal radial glia. In a forebrain  
41 conditional Eml1 mutant model and human patient cells, primary cilia and centrosomes are  
42 altered. Microtubule dynamics and cell cycle kinetics are also abnormal in mouse mutant  
43 radial glia. By rescuing microtubule formation in Eml1 mutant embryonic brains, abnormal  
44 radial glia delamination and heterotopia volume were significantly reduced. Thus, our new  
45 model of subcortical heterotopia reveals the causal link between Eml1's function in  
46 microtubule regulation and cell position, both critical for correct cortical development.

## 47 **Keywords**

48 Cortical development; brain malformation; microtubule; primary cilia; centrosome; cell cycle

## 49 **Introduction**

50 Cortical development is finely regulated to result in the formation of a functional cerebral  
51 cortex required for advanced cognitive functions such as perception and language. At the  
52 onset of neurogenesis, neuroepithelial cells (NECs) give rise to apical progenitors named  
53 radial glial cells (RG), that become the predominant neuronal progenitor cell type, able to  
54 self-renew but also give birth to post-mitotic neurons directly or indirectly *via* basal  
55 progenitors (intermediate progenitors or basal RG) (Götz & Barde, 2005; Noctor et al., 2001,  
56 2004). They are highly polarized cells with a short apical process that faces the ventricle and  
57 terminates in an enlarged apical domain where a primary cilium (PC), docked to a basal body  
58 (modified centrosome), protrudes into the embryonic cerebrospinal fluid (eCSF) to act as a  
59 signaling hub, sensing secreted molecules. RG also possess a long basal process that crosses  
60 the entire cortical wall and acts as a support for neuronal migration, before terminating at the  
61 pial surface (Rakic, 1972). RG somata are restricted to the ventricular zone (VZ) and exhibit  
62 interkinetic nuclear migration (INM), a process that defines the cell cycle-dependent  
63 movement of the nucleus within the VZ. More precisely, nuclei move in G1 to reach the more

64 basal part of the VZ to undergo S-phase and then re-descend apically in G2 to undergo  
65 mitosis at the ventricular surface (Sauer & Walker, 1959). INM relies on the actin and  
66 microtubule (MT) cytoskeletons, as well as motor proteins such as kinesin and dynein (Spear  
67 & Erickson, 2012; Tsai et al., 2010). Genetic mutations can alter RG in different ways,  
68 affecting cortical development and leading to cortical malformations (Romero et al., 2018;  
69 Stouffer et al., 2016).

70 Mutations in microtubule (MT) associated proteins can cause cortical malformations (Romero  
71 et al., 2018; Stouffer et al., 2016). We and others have identified *Echinoderm microtubule*  
72 *associated protein like 1* (*EML1*, also known as *EMAPLI*) mutations associated with human  
73 ribbon-like Subcortical heterotopia (SH) (Kielar et al., 2014; Shaheen et al., 2017). Patients  
74 with compound heterozygous, or homozygous mutations in *EML1* exhibit large clusters of  
75 abnormally positioned neurons within the white matter (Kielar et al., 2014; Shaheen et al.,  
76 2017). Patients may also present hydrocephalus, polymicrogyria, megalencephaly and corpus  
77 callosum pathology (Kielar et al., 2014; Markus et al., 2021; Oegema et al., 2019; Shaheen et  
78 al., 2017). Defects are associated with severe epilepsy, intellectual disability, and/or  
79 psychomotor developmental delay (Kielar et al., 2014; Oegema et al., 2019). *Eml1* mutations  
80 were also originally identified in a spontaneously arisen *Heterotopic Cortex* (*HeCo*) mouse  
81 model (Kielar et al., 2014). To our knowledge, *Eml1/EML1* is the only known gene found  
82 mutated in both human patients and rodent models with an SH phenotype (Bizzotto &  
83 Francist, 2015; Collins et al., 2019; Grosenbaugh et al., 2020; Kielar et al., 2014; Uzquiano et  
84 al., 2019). The EML1 protein, a member of the EMAP family, binds to MTs and has an N-  
85 terminal domain with a coiled coil motif and a C-terminal region with a tandem  $\beta$ -propeller  
86 structure (Richards et al., 2015). However, its role during neurodevelopment has remained  
87 elusive.

88 In the *HeCo* mouse, the spontaneous mutation in *Eml1* resulted from an insertion of a  
89 retrotransposon in an intron towards the end of the gene, leading to the absence of full-length  
90 transcripts and the presence of small quantities of chimeric transcripts (Kielar et al., 2014). In  
91 this model, it was shown that RG distribution is abnormal during cortical development. Many  
92 of these cells were found in basal locations in the cortex (e.g. the intermediate zone and  
93 cortical plate), hence proliferating outside the VZ and unable to act as a proper support for  
94 neuronal migration from the VZ (Kielar et al., 2014). RG detachment may hence be the  
95 primary event leading to heterotopia formation. It is important to further understand why

96 *Eml1* mutant RG detach, especially since similar mechanisms may contribute to basal radial  
97 glia (bRG) production in gyrencephalic brains (Borrell & Götz, 2014; Penisson et al., 2019).

98 Previously, apical extremity defects were revealed in *HeCo* RG, notably the PC did not form  
99 correctly, shown in both mutant murine and human progenitor cells (Bizzotto et al. 2017;  
100 Jabali et al. 2022; Markus et al. 2021; Uzquiano et al. 2019). We showed that *Eml1* full  
101 knockout reproduces heterotopia in mice, as well as RG detachment, but some lethality was  
102 observed, as well as hydrocephalus (Collins et al., 2019). In this study, we produced *Eml1*  
103 conditional knockout (cKO) mice with a forebrain-specific inactivation of *Eml1*, also  
104 revealing severe heterotopia but without hydrocephalus. In this new model, we focused on  
105 subcellular and cellular RG alterations in early and mid-corticogenesis to understand  
106 pathogenic mechanisms which may lead to heterotopia formation. Assessing centrosomes *in*  
107 *vitro* and in brain sections, we determined that their structure is affected in both human and  
108 mouse RG, impacting MT nucleation. This important phenotype may precede PC defects and  
109 RG apical detachment in early corticogenesis. By artificially stabilizing MT in embryonic  
110 brains at early stages of corticogenesis, we were able to partially inhibit RG delamination and  
111 reduce heterotopia volume, demonstrating a causal relationship between MT physiology,  
112 ectopic RG and heterotopia formation. With these data, we reveal new roles for *Eml1* in early  
113 cortical development, whilst unveiling key cellular patho-mechanisms contributing to the  
114 early onset of SH formation.

## 115 **Materials and Methods**

### 116 **Animals**

117 Research was carried out conforming to national and international directives (directive CE  
118 2010/63 / EU, French national APAFIS n° 23424; 46509) with protocols followed and  
119 approved by the local ethical committee (Charles Darwin, Paris, France). Mice were housed  
120 with a light/dark cycle of 12 h (lights on at 07:00). Males and females were used in all  
121 analyses.

### 122 **Generation of *Eml1* cKO animals**

123 The *Eml1* mutant mouse line was established at the PHENOMIN MCI/ICS (Mouse Clinical  
124 Institute - Institut Clinique de la Souris, Illkirch, France; <http://www-mci.u-strasbg.fr>), in the  
125 framework of funding from the French Rare Disease Foundation (Collins et al., 2019).  
126 The *Eml1* mutant line was generated and analysed on the mouse genetic background

127 C57BL/6N (B6N). LoxP sites surrounding exon 8 allowed conditional knockout. *Eml1* cKO  
128 mice were generated by crossing with *Emx1*-Cre knock-in animals (Gorski et al., 2002).  
129 Homozygote *Eml1*-Flox mice (*Eml1* fl/fl) were crossed with homozygote *Eml1*-Flox mice  
130 also heterozygote for *Emx1*-Cre (Gorski et al., 2002) (*Eml1* fl/fl x *Eml1* fl/fl, *Emx1*-Cre/+).  
131 All mice were housed in the IFM institute animal facility or at the CDTA, Orléans, France.

## 132 **Crosses and genotyping**

133 *Eml1* flox/flox animals were crossed with *Eml1* flox/flox-*Emx1*Cre/+ animals. Females were  
134 placed in the male cage and the following morning the presence of a vaginal plug was  
135 observed and considered to be embryonic day 0.5 (E0.5). Embryonic brains were collected at  
136 the indicated times.

137 Genotyping primers used to detect Cre were:

138 Cre 1: GAACCTGATGGACATGTTTCAGG

139 Cre 2: AGTGCGTTCGAACGCTAGAGCCTGT

140 Primers used to detect the floxed *Eml1* allele were:

141 Primer Lf: GAAAACGTGCTTTGCTGTGTACATAGG

142 Primer Er: CACCCACTGAAGAAATGACTGGCAG

## 143 **Antibodies**

144 Primary antibodies used were: mouse anti-BrdU (ThermoFisher Scientific Cat# B35141,  
145 RRID:AB\_2536441 MobU-1, 1:100), rabbit anti-Pax6 (Covance Cat# PRB-278P,  
146 RRID:AB\_291612, 1:300), rabbit anti-Tbr2 (Abcam Cat# ab23345, RRID:AB\_778267,  
147 1:300), mouse anti-Ki-67 (BD Biosciences Cat# 556003, RRID:AB\_396287, 1:200), rabbit  
148 anti-PCNA (Proteintech Cat# 10205-2-AP, RRID:AB\_2160330), mouse anti-GM130 (BD  
149 Biosciences Cat# 610822, RRID:AB\_398141, 1:300), mouse anti-Cep170 (ThermoFisher  
150 Cat# 41-3200, RRID:AB\_2533502, 1: 500), mouse anti- $\gamma$ -tubulin (Sigma-Aldrich Cat#  
151 T6557, RRID:AB\_477584, 1:400), mouse anti- $\alpha$ -tubulin (Sigma-Aldrich Cat# T9026,  
152 RRID:AB\_477593, 1:500), rabbit anti-Arl13b (Proteintech Cat# 17711-1-AP,  
153 RRID:AB\_2060867, 1:400), mouse anti-*Eml1* 3E8 (Santa Cruz Biotechnology Cat# sc-  
154 100938, RRID:AB\_1122523, 1:500), rabbit anti-*Eml1* C3 (GeneTex Cat# GTX100252,  
155 RRID:AB\_1240763, 1:500), goat anti-Sox2 (Santa Cruz Biotechnology Cat# sc-17320,  
156 RRID:AB\_2286684, 1:500) and rabbit anti-GFP (ThermoFisher Cat# A-6455,  
157 RRID:AB\_221570, 1:2000), rabbit anti-Pericentrin (Abcam Cat# ab4448,

158 RRID:AB\_304461), rabbit anti-Satb2 (Abcam Cat# ab92446, RRID:AB\_10563678, 1:1000).  
159 For Neuro-2A cells: Streptavidin Alexa Fluor 488 conjugate (Life Technologies, S32354,  
160 1:5000, RRID:AB\_2315383), Myc-tag (Cell Signaling, 2278, 1:400, RRID:AB\_490778), and  
161  $\gamma$ -tubulin (Sigma-Aldrich, T5326, 1:200, RRID:AB\_532292) were used.

162 Secondary antibodies used for immunohistochemistry and immunocytochemistry were goat  
163 anti-rabbit Alexa Fluor 555 (Cell Signaling Technology Cat# 4413, RRID:AB\_10694110),  
164 goat anti-mouse Alexa Fluor 633 (Thermo Fisher Scientific Cat# A-21052,  
165 RRID:AB\_2535719), Streptavidin conjugated Alexa Fluor 488 (Invitrogen, S32354), goat  
166 anti-rabbit Alexa 488 (ThermoFisher Cat#A-11008; RRID: AB\_143165), goat anti-mouse  
167 Alexa 488 (ThermoFisher, Cat#A28175; RRID: AB\_2536161), goat anti-rat Alexa 568  
168 (ThermoFisher Cat# A-11006; RRID: AB\_141373, 1:800), goat anti-rabbit Alexa 568  
169 (ThermoFisher, Cat# A-11011; RRID: AB\_143157; 1:800), goat anti-mouse Alexa 633  
170 (ThermoFisher, Cat# A-21050; RRID: AB\_2535718; 1:800), goat anti-rabbit Alexa 633  
171 (ThermoFisher, Cat# A-21070, RRID: AB\_2535731; 1:800). Secondaries used for Western  
172 blot were Dylight anti-mouse 800 (ThermoFisher, Cat#SA5-35521; RRID: AB\_2556774,  
173 1:5000), anti-rabbit 680 (ThermoFisher, Cat# 35568, RRID: AB\_614946, 1:5000), anti-rabbit  
174 800 (ThermoFisher, Cat#SA5-35571; RRID: AB\_2556775, 1:5000).

## 175 **Plasmids**

176 Plasmids used were BLBP-GFP (Kielar et al, 2014) for *in utero* electroporation, CMV-  
177 3xFlag-EML1 (Uzquiano et al, 2019) and YFP-EML4 (Richards et al, 2015) for  
178 immunoprecipitation. For BioID, full-length mouse Eml1 and Eml1\*T243A cDNAs were  
179 cloned into the pcDNA3.1 mycBioID (Addgene#35700) vector. Retention using selective  
180 hooks (RUSH (Boncompain et al. 2012)) was performed with SSTR3-GFP (generated in  
181 Franck Perez's lab) and PKD2-GFP (kindly provided by Dominic Norris' lab, London UK).

## 182 **Embryonic brain collection and sectioning**

183 Females were sacrificed by cervical dislocation and embryos were collected. Brains were  
184 fixed overnight with paraformaldehyde (PFA) 4% and then rinsed and stored with phosphate  
185 buffered saline 1X (PBS). For vibratome sectioning: brains were placed in an inclusion of  
186 10% sucrose and 7.5% agarose in PBS 1X. Brains were cut in 70  $\mu$ m thick coronal sections  
187 using a vibrating blade microtome (Leica VT1000 S). For cryostat sectioning, brains were



188 embedded in OCT (Eprelia, Ref 6502) and frozen. Brains were cut in 20  $\mu\text{m}$  thick coronal  
189 sections using a cryostat (Cryostar NX70, HOMVDP, Microm).

### 190 **Cresyl-violet labeling**

191 Cresyl violet staining was performed on sections mounted on Superfrost slides  
192 (ThermoFisher). Sections were treated 5 minutes with EtOH 100%, then 5 min with EtOH  
193 95% and 2 min with EtOH 70%. Slices were rinsed in water and then incubated in Cresyl-  
194 Violet solution (Sigma 46597MJ) for 8 minutes and then with water (1 min), EtOH 70% (2  
195 min), 95% (1 min) and 100% (3 min). After 5 minutes in xylene, they were mounted with  
196 Eukitt medium.

197 Sections were analyzed at room temperature with a brightfield microscope (Provis; Olympus)  
198 using a charge-coupled device (CCD) camera (CoolSNAP CF; Photometrics) with 2 $\times$  (NA =  
199 0.08), 4 $\times$  (NA = 0.13) and 10X (NA=0.30) objectives. Minimum contrasts were adjusted  
200 using Photoshop software (Adobe).

### 201 **Protein lysates and dosage**

202 Embryonic cortices were collected, and lysis of each embryonic cortex was performed  
203 individually, by resuspending the tissue continuously with lysis buffer for a period of 1h at  
204 4°C. The lysate was then centrifuged (30 min, 15000 rcf, 4°C), the supernatant was collected,  
205 and the protein concentration was measured using the BCA protein assay kit (ThermoFisher)  
206 and the BertholdTech Mithras ELISA microplate reader.

207

### 208 **Western blot**

209 Samples were denatured with 2X NuPAGE LDS Buffer (ThermoFisher) for 10 min at 70°C.  
210 Denaturing electrophoresis was performed on a 4%–12% Bis-Tris Gel with MOPS SDS  
211 running buffer for 2h at 110V. Proteins were transferred onto nitrocellulose membranes for 1h  
212 at 110V and 4°C in a Tris-Glycine transfer buffer (Tris 25 mM, Glycine 192 mM, ethanol  
213 10%). After protein transfer, the membranes were stained with Ponceau red to check the  
214 transfer quality. The membranes were extensively washed with distilled water, followed by a  
215 60 min incubation in 1X TBST (100 mM Tris pH 7.5, 150 mM NaCl, 10% ethanol, 0.05%  
216 Tween) + 5% non-fat milk. Incubation for 45 min in the dark with the secondary antibody  
217 (DyLight, see above) was performed to identify non-specific binding sites. The primary  
218 antibody was incubated overnight (O/N) at 4°C, and abundantly washed with 1X TBST,

219 followed by incubation with the secondary antibody (see above). After extensive washes in  
220 TBST then with 1X TBS, the membranes were scanned using an Odyssey (Li-Cor) infrared  
221 scanner, with ImageStudio software.

## 222 **In utero electroporation (IUE)**

223 Timed-pregnant mice (E12.5 to E14.5) were anesthetized with isoflurane (4% during  
224 induction and 2–2.5% during surgery) and embryos were revealed within the intact uterine  
225 wall after sectioning the abdomen. Embryos were constantly hydrated with NaCl 0.9% (B.  
226 Braun). A solution containing Blbp-GFP plasmid DNA (1 µg/µl, Blbp-promoter specific for  
227 RG) and 20 % w/v fast green in sterile endo-free water was injected in the lateral ventricles of  
228 the embryos. Forcep electrodes (System CUY650P5 NepaGene Co) were placed around the  
229 embryo head at a 45° angle and plasmids electroporated by discharging a 4,000-µF capacitor  
230 charged to 35 V (five electric pulses of 50 ms with 950 ms intervals) with a CUY21  
231 NepaGene electroporator. The embryos were then placed back in the abdominal cavity for 24  
232 h prior to subsequent analyses.

233 Embryonic heads were harvested and fixed overnight with 4% PFA at 4°C. Brains were  
234 extracted, washed in PBS and cryoprotected overnight serially in 15% and 30% sucrose.  
235 Brains were embedded in an embedding chamber using cryomedium Neg-50 (Epredia, Ref  
236 6502), frozen under isopentane and dry ice, and cryo-sectioned at 20 µm with a Cryostar  
237 NX70 (HOMVPD, Microm). Brain sections were fluorescently immunolabelled (see below)  
238 with antibodies detecting Pax6 and GFP in electroporated progenitors. Images were acquired  
239 at room temperature with a TCS Leica SP5-II confocal microscope, with analyses focused on  
240 the future somatosensory cortex. 40X (NA = 1.25–0.75) and 100 X (NA=1.44) objectives  
241 were used controlled by LAS-AF software for acquisition (Leica). ImageJ was used for cell  
242 counting.

## 243 **EpoD treatment in mice**

244 Females were injected intraperitoneally with 20mg/kg Epothilone D (EpoD, Abcam) at E11.5,  
245 E12.5 and sacrificed at E13.5 (for vibratome sectioning and immunohistochemistry) or E18.5  
246 (for 3D imaging). EpoD was stored in PBS 1X and the exact needed volume was resuspended  
247 in saline 37°C in a final volume of 200 µL. For control injections, 200 µL of saline 37°C was  
248 injected at the indicated times.

## 249 **Immunohistochemistry**

250 Immunohistochemistry for all other experiments was performed on floating brains slices.  
251 These were permeabilized with 1X PBST (0.1% Triton X-100) for 15 min. After washes,  
252 blocking was performed for 1 h at room temperature (RT) with 1X PBS containing 10%  
253 normal goat serum (NGS) and 0.1% Triton X-100 before incubation overnight (O/N) at 4°C  
254 with the primary antibody. After extensive washes, sections were incubated with the  
255 secondary antibodies for 2 h at RT protected from the light. This was followed by 10 min  
256 incubation in Hoechst stain (ThermoFisher, 1:10000) prior to washing with 1X PBS. Brain  
257 slices were mounted using Fluoromount G (Invitrogen). Images were acquired at room  
258 temperature with a TCS Leica SP5-II confocal microscope, with analyses focused on the  
259 future somatosensory cortex. Fluorochromes are as described above in the antibody section.  
260 40X (NA = 1.25–0.75) and 100 X (NA=1.44) objectives were used controlled by LAS-AF  
261 software (Leica). Minimum contrast adjustment was performed using ImageJ software.

262 For Tbr2, Ki67 and PCNA labelling, antigen retrieval was performed by incubating the  
263 sections in sodium citrate 10 mM pH 6 at 95°C for 20 min and allowing them to cool down  
264 before blocking.

265 For EdU and BrdU labelling after permeabilization, DNA was denatured with hydrochloric  
266 acid (HCl) 2N treatment during 30 min at 37°C, followed by washes and blocking. EdU was  
267 labelled using a click it EdU kit 647 following manufacturer's instructions (C10340,  
268 ThermoFisher).

## 269 **3D visualization of the heterotopia**

270 E18.5 embryonic brains were dissected and fixed in 4% PFA overnight. They were then  
271 incubated in PBS1X gelatin 0.2% Triton 0.5% (PBSGT) at RT for 24 hours. Anti-Satb2  
272 antibody was diluted in PBSGT containing 0.1% saponin at 37°C for at least 5 days, after  
273 which the brains were washed six times in PBSGT at RT. The next day, secondary antibodies  
274 were diluted in PBSGT+saponin and incubated at 37°C for at least 2 days. All steps were  
275 performed on a rocking platform or wheel. Immunolabeled brains were embedded in 1.5%  
276 low-melting agarose (in 1% ultrapure Tris-acetate-EDTA solution). The embedded samples  
277 were cleared according to a modified version of the original iDISCO+ protocol (Renier et al.,  
278 2016). Samples were dehydrated by consecutive treatment with increasing concentrations of  
279 methanol and finally incubated in 1 volume of methanol / 2 volumes of dichloromethane

280 (DCM, Sigma 270997-12X100ML). The samples were then washed twice in 100% DCM.  
281 Finally, samples were incubated in di-benzyl ether (DBE, Sigma 108014-1KG) overnight. For  
282 3D imaging, cleared samples were imaged on a light sheet microscope (LaVision Biotec)  
283 equipped with a sCMOS camera (Andor Neo). Samples were imaged at room temperature in  
284 DBE. Inspector microscope control software was used. Scans were taken at 1.25X zoom  
285 magnification. Imaris (Bitplane, <http://www.bitplane.com/imaris/imaris>) was used for 3D  
286 reconstruction, snapshots and movies.

## 287 **Mouse neuronal progenitor primary cell culture**

288 The neuronal progenitor cell cultures were adapted from (Sun et al., 2011) giving highly  
289 enriched populations of Pax6(+) cells. For this, 6-well cell culture plates were coated with  
290 Poly-D-lysine (PDL, P6407, Sigma Aldrich) 2  $\mu\text{g}/\text{cm}^2$  in sterile 1X PBS, O/N, at 37 °C and 5  
291 % CO<sub>2</sub>. The following day, the PDL was removed, and the plates were coated with 1  $\mu\text{g}/\text{cm}^2$   
292 fibronectin (F1141, Sigma Aldrich) in sterile 1X PBS. E14.5 timed-pregnant mice were  
293 sacrificed by cervical dislocation and the uterus was placed in ice cold basal medium  
294 (DMEM/F12 Hams, 21041, ThermoFisher, 1% Pen-Strep (Gibco), 2.9 mg/ml glucose and 1.2  
295 mg/ml sodium bicarbonate). The embryos were collected and the cortex from both  
296 hemispheres was dissected and kept at 4°C in basal medium. The medium was removed and  
297 substituted by pre-warmed sterile complete medium (basal medium complemented with 1X  
298 B27 without vitamin A (12589-010, Gibco), 20 ng/ml of EGF (E9644, Sigma Aldrich) and 20  
299 ng/ml of FGF (F0291, Sigma Aldrich). The tissue was dissociated, and each sample was  
300 centrifuged (3 min, 1000 rcf). The medium was removed and substituted by fresh pre-warmed  
301 complete medium followed by re-suspension of the cells.  $1 \times 10^5$  cells were plated in coated 6-  
302 well culture plates. The cells were split once at seven days in vitro (DIV) before performing  
303 experiments. Half of the culture medium was changed by fresh complete medium every 2  
304 days for one week. For splitting, cells were washed with pre-warmed Versene (Gibco),  
305 followed by a 3 min incubation with pre-warmed StemPro Accutase (Gibco) at 37°C. Cells  
306 were plated ( $6-8 \times 10^5$ ) on coated 14 mm glass coverslips and cultured for 2 DIV for  
307 immunocytochemistry experiments.

## 308 **Immunocytochemistry**

309 Cells were washed in 1X PBS prior to fixation with 4% w/v PFA in 0.1 M phosphate buffer,  
310 pH 7.4, for 15 min at RT or fixed with methanol at -20°C. The cells were extensively washed

311 for 15 min in PBST (Triton X-100 0.1% in 1X PBS). Incubation with blocking solution (10%  
312 NGS, ThermoFisher, 0.1% Triton X-100 in 1X PBS) was performed for 1 h at RT and  
313 primary antibodies were applied for 2h at RT or O/N at 4°C (see above for antibodies). The  
314 cells were extensively washed with blocking solution and secondary antibodies were  
315 incubated for 2h at RT in the dark. After washes, Hoechst (1:10000, ThermoFisher) was  
316 applied for 15 min at RT in the dark. The cells were extensively washed in PBS and the  
317 coverslips mounted with Fluoromount G (Southern Biotechnology). Images were acquired at  
318 room temperature with a TCS Leica SP5-II confocal microscope as above.

### 319 **RUSH trafficking experiments**

320 Retention using selective hooks (RUSH (Boncompain et al., 2012)) was performed with  
321 plasmids SSTR3-GFP (lab) and PKD2-GFP. Plasmids were individually transfected in  
322 neuronal progenitor Pax6+ cells in culture, using Lipofectamine 3000 (Invitrogen, L3000-  
323 008) following manufacturer's instructions. An avidin concentration of 0.28 µg/mL was  
324 added to block biotin already present in the DMEM F12 medium (Invitrogen, 21041025)  
325 (Boncompain et al., 2021). After 24h, biotin at a concentration of 40µM in new medium was  
326 added for a given time duration (0, 30, 60 and 90 minutes) and cells were fixed with 4% PFA  
327 at RT for 15 min. Co-immunolabelling with GM130 and Arl13b antibodies as described  
328 above was performed to assess the concentration of the RUSH protein respectively in the  
329 Golgi Apparatus (GA) and primary cilia (PC) over time. Images were acquired at room  
330 temperature with a TCS Leica SP5-II confocal microscope as above and analyzed using  
331 Image J.

### 332 **Microtubule (MT) regrowth assay**

333 Primary cultures of mouse neuronal progenitor cells were plated on coated 14 mm glass  
334 coverslips and placed directly on ice, then incubated for 40 min to allow disassembly of the  
335 MT cytoskeleton. The cells were then placed at 37°C for the indicated times (1 min or 2 min)  
336 and immediately fixed with methanol at -20°C. Immunolabelling for pericentrin and α-tubulin  
337 were then performed as described above to analyze MT regrowth at the centrosomes. Images  
338 were acquired at room temperature with a TCS Leica SP5-II confocal microscope as above  
339 and analyzed using Image J.

### 340 **Human cells and electron microscopy (EM)**

341 Centrosomes were identified and analyzed in previously generated EM images of human  
342 cortical progenitors (Uzquiano et al. 2019, Jabali et al. 2022). Control cells were Ctrl1: id-  
343 number B7\_028#4, female origin; Ctrl2: catalog ID GM08680, male origin. EML1  
344 heterotopia patients were P135 (T243A compound heterozygous mutations) and P3489  
345 (homozygous W225R mutations) (Kielar et al., 2014).

346 Progenitor cells were previously produced, fixed and imaged with an electron microscope  
347 (Philips CM100), digitalized with a CDD camera (Gatan Orius). Images were analyzed using  
348 ImageJ. In this study, centrosome aspect and numbers were assessed.

## 349 **Cell cycle analysis**

### 350 **EdU and BrdU injections**

351 BrdU (10 mg/ml) and EdU (5 mg/ml) were dissolved with 1X PBS. Intraperitoneal injections  
352 of the appropriate volume of EdU and BrdU solutions were carried out for an injection of 50  
353 mg/kg of EdU and 50 mg/kg of BrdU (one hour after the first injection). 1.5h after the first  
354 injection, the pregnant mouse was euthanized by cervical dislocation and brains of embryos  
355 were collected. After immunolabeling for EdU, BrdU and Pax6 on embryonic floating coronal  
356 brain sections, RG were assessed according to their S-phase state (Harris et al., 2018;  
357 Martynoga et al., 2005): The confocal SP5 microscope was used as already mentioned above.  
358 Pax6 (+)Edu(+)BrdU(-) cells were considered to have left S-phase, Pax6(+)Edu(-)BrdU(+)  
359 cells to have entered in S-phase and Pax6(+)Edu(+)BrdU(+) to be still in S-phase.

360 Considering that in a population of proliferating asynchronous cells, the fraction of cells in a  
361 given phase of the cell cycle is directly proportional to the duration of that phase relative to  
362 the total duration of the cell cycle (Nowakowski et al., 1989) we could thus calculate S-phase  
363 length  $T_s = (\text{EdU}^+; \text{BrdU}^+ \text{ cells} / \text{EdU}^+; \text{BrdU}^- \text{ cells})$ . Also, because RG are cycling cells, we  
364 could estimate their cell cycle duration using the formula  $T_c = T_s / (\text{BrdU}^+ / \text{Pax6}^+ \text{ cells})$ . In more  
365 details: the ratio between the duration of one period of the cell cycle and that of another  
366 period is equal to the ratio between the number of cells in the first period and the number of  
367 cells in the second period (Nowakowski et al., 1989). The sequential exposure of proliferating  
368 cells to EdU and BrdU allowed us to differentiate defined cell populations. Specifically,  
369 progenitors are exposed to EdU in vivo at  $T = 0\text{h}$  so that all cells in S phase at the start of the  
370 experiment are labeled with EdU. At  $T = 1\text{h}$ , cells are exposed to BrdU to label all cells in S  
371 phase at the end of the experiment. Cells still in S phase are also labelled with EdU. The

372 interval during which cells can incorporate EdU but not BrdU (T') is 1h. Cells from the initial  
 373 EdU-labeled S-phase cohort will leave S-phase at a constant rate during the T' interval. This  
 374 outgoing fraction will be labeled by EdU but not by BrdU. Consequently, the ratio between  
 375 the number of EdU+BrdU- and EdU+BrdU+ cells is equal to the ratio between T' (which  
 376 equals 1h) and Ts (Shibui et al., 1989). Thus,  $T_s = \text{number of EdU+BrdU+} / \text{EdU+BrdU- cells}$   
 377 and  $T_c = T_s / (\text{BrdU+} / \text{Pax6+ cells})$ .

### 378 **Dual labelling for Ki67 and PCNA**

379 The method was adapted from Fousse et al (Fousse et al., 2019). The confocal SP5  
 380 microscope was used as already mentioned above. Cells with punctate PCNA in the nucleus  
 381 and diffuse Ki67 were considered in S-phase. Cells with punctate Ki67 and diffuse PCNA  
 382 were counted as cells in G1 phase. Nuclei with both Ki67 and PCNA in a diffuse pattern were  
 383 considered as G2/M cells. Cells were counted using the plugin cell counter in ImageJ.

### 384 **BioID (Proximity Dependent Biotin Identification)**

#### 385 **Cloning**

386 Full-length mouse *Eml1* and *Eml1\*<sup>T243A</sup>* cDNAs were cloned into pcDNA3.1 mycBioID  
 387 (Addgene#35700) vector using the following primers:

Primer Name	5' to 3'
Eml1_BioID_N_ F	CTGTGCTGGATATCTGCAGAATTCATGGAGGACGGCTTCTCC
Eml1_BioID_N_ R	TGATCAGCGGTTTAAACTTAAACTTAAGCTTCTAAATGACTCGCCAC TGC

388

### 389 **BioID (Proximity Dependent Biotin Identification) Analysis**

390 Mouse Neuro2A cells (ATCC CCL-131) were transiently transfected 40 µg BioID constructs  
 391 with Polyethylenimine (PEI) (Polysciences Inc., Cat. #23966) and after 24 hours, cells were  
 392 incubated overnight in the presence of 0.05 mM D-biotin (Life Technologies, Cat. #B1595),  
 393 followed by cell lysis in a lysis buffer (150 mM NaCl, 0.5% SDS, 2% NP40, 1mM EDTA,  
 394 10mM IAA, 10 mM Tris pH 7.6 and Protease Inhibitor Cocktail, Roche, Cat.#11836170001).  
 395 The lysates were centrifuged at 14,000g for 10 min at 4°C, and the protein concentrations

396 were measured using a bicinchoninic acid (BCA) assay (BCA Protein Assay Kit (Thermo  
397 Scientific, Cat. #23225). Equal amounts of protein lysates from different conditions were  
398 incubated with streptavidin beads (Pierce® Streptavidin Plus UltraLink® Resin, Thermo  
399 Scientific, Cat.#53117) overnight at 4°C. The bound proteins were washed with several wash  
400 buffers respectively for 10 min, wash buffer 1 (2% SDS), wash buffer 2 (1% Triton X-100,  
401 2% sodium deoxycholate, 1mM EDTA, 50 mM NaCl, 50 mM HEPES pH 7.5), wash buffer 3  
402 (1% Triton X-100, 0.5% NP-40, 0.5% sodium deoxycholate, 1mM EDTA, 50 mM NaCl, 10  
403 mM Tris pH 8.1) and wash buffer 4 (50 mM NaCl, 50 mM Tris pH 7.4).

404 To identify biotinylated proteins by mass spectrometry (MS), on bead digestion was  
405 performed. Proteins on the beads were reduced with 100 mM DTT in 50 mM ammonium  
406 bicarbonate buffer at 56°C for 45 min and alkylated with 100 mM iodoacetamide at RT in the  
407 dark for 30 min. MS grade trypsin (Pierce) was added to the beads for overnight digestion at  
408 37°C. The resulting peptides were purified using C18 StageTips. Finally, the eluted peptides  
409 were analyzed by a Thermo Fisher Scientific Q-Exactive LC-MS/MS mass spectrometer. This  
410 experiment was performed three independent times.

411 The raw data were processed using Proteom Discoverer 2.3 (Thermo Fisher Scientific) and  
412 searched against the UniProt *Mus musculus* database (accessed August 2022) with Sequest  
413 HT search engine with tryptic digest specificity, allowing maximum two missed cleavage,  
414 precursor mass tolerance 15 ppm, and fragment mass tolerance 0.05 Da (Liu et al., 2020).  
415 SAINTexpress analysis was performed using three biological replicates (Teo et al., 2014).  
416 Biotinylated proteins of negative control, transfected without DNA, were analyzed to define  
417 non-specific interactions. Saint probability score  $\geq 0.6$  was used to define the proximal  
418 interactors of EML1 and EML1\*T243A. The final protein lists were analyzed using the  
419 STRING v11.5 database (Szklarczyk et al., 2021) and g:Profiler annotation server (Raudvere  
420 et al., 2019). Selected protein interactions were visualized using Cytoscape 3.9.1 (Shannon et  
421 al., 2003).

## 422 **Immunocytochemistry of Neuro2A cells**

423 For immunofluorescence staining, Neuro2A cells (ATCC CCL-131) were transfected with  
424 Lipofectamine 3000 (Invitrogen). Two days after transfection, the cells were fixed with 4%  
425 paraformaldehyde (PFA). The antibodies and their dilutions used were as follows:  
426 Streptavidin Alexa Fluor 488 conjugate (Life Technologies, S32354, 1:5000,



427 RRID:AB\_2315383), Myc-tag (Cell Signaling, 2278, 1:400, RRID:AB\_490778), and  
428 Gamma-Tubulin (Sigma-Aldrich, T5326, 1:200, RRID:AB\_532292). Secondary antibodies  
429 were DAPI (359 nm), Alexa Fluor 488 (Invitrogen, S32354), Alexa Fluor 555 (Cell  
430 Signaling, 4413), Alexa Fluor 633 (Invitrogen, A21052). Vectashield mounting medium was  
431 used (Vector Laboratories, H-1200-10)

432 After fixation, images were acquired at room temperature with a Leica DMI8 / SP8 TCS DLS  
433 laser scanning confocal microscope: HyD detectors provide signal collection in channels, then  
434 acquired using a DFC365 FX camera (version FCAM2 V1.0.10). A 63× Plan Apo 1.4 NA oil-  
435 immersion objective was used controlled by LAS-X software (Leica).

436

### 437 **Co-immunoprecipitation experiments**

438 For co-immunoprecipitation (IP) experiments, Neuro2A cells were co-transfected with CMV-  
439 3xFlag-EML1 (Uzquiano et al, 2019) and YFP-EML4 (Richards et al, 2015) plasmids, or  
440 CMV-3xFlag vector only (Uzquiano et al, 2019) with YFP-EML4 (Richards et al, 2015).  
441 After 24 h in culture, cells reaching 70%–80% confluence were transfected using a ratio of  
442 1:3 DNA and PEI, respectively (10 µg of DNA and 30 µg of PEI, Polysciences). After 48 h,  
443 cells were recovered and washed twice with 1 X PBS and lysed by rotation for 20 min at 4°C  
444 in 150 µl of RIPA buffer (50 mM Tris-HCl, pH 8, 100 mM NaCl, 1 mM EDTA, 0.1% SDS,  
445 1% Nonidet P-40, 0.5% sodium deoxycholate and Protease inhibitor cocktail). The samples  
446 were centrifuged at 14000 rcf. for 15 min at 4°C. Protein G Sepharose beads (Sigma Aldrich)  
447 were diluted 1/10 in TNE buffer (50 mM Tris-HCl pH 7.4, 100 mM NaCl, 5 mM EDTA) and  
448 60 µl of diluted beads were used for each IP experiment. The beads were extensively washed  
449 with 1 x RIPA buffer, followed by centrifugation (12000 rcf., 4°C, 30 s). A pre-clearing step  
450 was performed by incubating the cell lysates with the already-washed beads on a rotating  
451 wheel at 4°C for 1 h 30 min. The samples were then centrifuged (12000 rcf., 4°C, 30 s) and  
452 the supernatant collected. The latter was incubated with the following primary antibodies (1  
453 µg): rabbit anti-GFP (A6455, Invitrogen), mouse anti-Flag (F1804, Sigma Aldrich), (O/N, 4°,  
454 rotating wheel). Afterward, these samples were incubated with 100 µl of diluted washed  
455 Protein G Sepharose beads (5 h, 4°C, rotating wheel). The unbound fraction was recovered  
456 after centrifugation (12000 rcf., 4°C, 30 s). 5x washes of the beads in 1 x RIPA buffer were  
457 performed before elution with NuPAGE LDS Buffer (Thermo Fisher), 10 min at 70°C. The  
458 bound fraction was recovered after centrifugation (12000 rcf., RT, 2 min). Western blots and  
459 immunodetection were performed as mentioned above.

## 460 **Image acquisitions**

461 As mentioned in the above methods, acquisitions of immunolabeled brain sections and plated  
462 cells were carried out using confocal microscopes Leica SP5 and SP8. For vibratome brain  
463 imaging a total of  $z=10\ \mu\text{m}$  was imaged and for cryostat a total of  $z=20\ \mu\text{m}$  was imaged. For  
464 cells a total of  $z=7\ \mu\text{m}$  was imaged. Hoechst (DAPI, 359 nm), Alexa Fluor 488 (Invitrogen,  
465 S32354), Alexa Fluor 555 (Cell Signaling, 4413), Alexa Fluor 633 (Invitrogen, A21052) were  
466 used.

## 467 **Image analysis**

468 Cell and element counting (Fig 1, Fig 2, Fig 3, Fig 4, Fig 6, Fig 7, Fig 8, Supp Fig 2) was  
469 performed using Image J. Fluorescence intensity (Fig 4, Fig 5, Fig 6, Supp Fig 4, Supp Fig 5)  
470 was measured using ImageJ. Images were acquired the same manner, with the same  
471 parameters. For sections, the analyzed region of interest (ROI) was 200 microns width and the  
472 total cortical wall in height, except for Ki67/PCNA analyses where the ROI was 100 microns.  
473 Imaris (Bitplane, <http://www.bitplane.com/imaris/imaris>) was used for 3D reconstruction,  
474 snapshots and movies (Fig 8, Supp Fig 1).

## 475 **Statistical analysis**

476 The sample size selection for experiments was based on both published and previous pilot  
477 studies considering the sensitivity of the applied approaches. When possible, data were  
478 collected and analysed in a blind manner to the experimenter. One main experimenter  
479 performed each experiment. Statistical tests were carried out using GraphPad Prism 9.  
480 Normality and homogeneity of variances were tested using either a D'Agostino-Pearson  
481 omnibus, Shapiro-Wilk or KS normality tests, or data distribution was assumed to be normal  
482 but this was not formally tested, depending on the number of samples. Significance was  
483 established with  $p\text{-value} < 0.05$ . For each experiment, the statistical test used (Mann Whitney  
484 or Two-way Anova) is described in the figure legend, as well as the number of individuals  
485 analyzed. Data were collected and processed randomly.

486

## 487 **Supplemental material**

488 This manuscript contains 5 Supplemental figures and 2 Supplemental videos.

489

## 490 **Results**

### 491 **Ectopic RG detachment and PC defects occur during early** 492 **embryonic cortical development in *Eml1* cKO mouse brains**

493 To study the role of *Eml1* in RG detachment linked to heterotopia formation, we generated a  
494 forebrain-specific *Eml1* cKO mouse model (Supplementary Figure 1 A). By crossing  
495 homozygote *Eml1*-Flox mice (*Eml1* fl/fl) with *Eml1*-Flox mice also heterozygote for *Emx1*-  
496 Cre (Gorski et al., 2002), homozygote forebrain-specific *Eml1* cKO (*Eml1* fl/fl *Emx1*-Cre/+) animals  
497 were obtained. Controls were Cre-negative *Eml1* fl/fl animals. 100% of *Eml1* cKO  
498 mice exhibit SH, as shown with cresyl violet staining at 8 weeks (Supplementary Figure 1 B),  
499 as well as *Satb2* staining at embryonic stage E18.5 and 3D visualization of the heterotopia  
500 (Supplementary Figure 1 C, Video 1 and 2). *Eml1* protein was shown to be absent by Western  
501 blot (WB, Supplementary Figure 1 D).

502 After confirming the presence of heterotopia in adult *Eml1* cKO animals, RG were  
503 characterized during development. Performing immuno-labelling for Pax6, a transcription  
504 factor marker of RG (Englund et al., 2005), on embryonic coronal brain sections at different  
505 developmental stages, the distribution of cells was analyzed throughout the cortical regions.  
506 At E12.5, no differences in the total count of Pax6 positive (+) cells, neither in the proportion  
507 of detached RG (outside the VZ) were observed in *Eml1* cKO brains (Figure 1 A-C)  
508 compared to controls. From E13.5, the proportion of detached Pax6+ cells was increased in  
509 *Eml1* cKO embryonic brains, as well as the total number of Pax6+ cells (Figure 1 A-C). This  
510 suggests that RG begin to detach from E12.5 to E13.5 in the absence of *Eml1*. Cortical wall  
511 thickness (CW) was unchanged until E15.5 when it was thicker in the *Eml1* cKO condition  
512 (Figure 1 D). VZ thickness compared to CW thickness was significantly reduced at E14.5 and  
513 E15.5 suggesting that the progenitor pool in the VZ is depleted over time (Figure 1 D).

514 Previously PC defects were observed in *HeCo Eml1* mutants (Bizzotto et al., 2017; Uzquiano  
515 et al., 2019), we hence assessed if they were defective at early- and mid-corticogenesis in  
516 *Eml1* cKO brains. *Arl13b* (a marker of PC) was immunodetected, revealing puncta at the  
517 ventricular surface. At E12.5, the total number of *Arl13b*+ puncta was not changed, but the  
518 mean length of PC was reduced in mutants (Figure 1 E-G). At E15.5, PC mean size was not  
519 significantly different, although a tendency for reduction was observed. However, the number  
520 of *Arl13b*+ puncta was decreased (Figure 1 H-J). These data suggest that PC defects are

521 present before observation of detached RG and that they are consistently observed in all *Eml1*  
522 mouse models.

523 Thus, these data suggest that Pax6<sup>+</sup> cells start to detach from E12.5 to E13.5, when an overall  
524 increased number of Pax6<sup>+</sup> RG is observed. Detachment correlates with a depletion of the VZ  
525 pool of RG during corticogenesis.

526 We further tested if RG detach in a stage-specific manner in *Eml1* mutant conditions. *In utero*  
527 *electroporation* (IUE) was performed to introduce the BLBP-GFP plasmid into RG at the  
528 ventricular surface at different stages. One day after IUE, embryos were sacrificed and  
529 immuno-labelling for Pax6 was performed to assess the percentage of electroporated RG in  
530 the VZ versus those outside the VZ (detached or ectopic progenitors). In the *Eml1* cKO an  
531 increased percentage of BLBP-GFP<sup>+</sup> Pax6<sup>+</sup> cells was found outside the VZ compared to the  
532 WT after IUE at E12.5 and sacrificed at E13.5 (Figure 2 A, B). There were correspondingly  
533 fewer cells observed in the VZ. From E14.5 to E15.5, a proportion of BLBP-GFP<sup>+</sup> Pax6<sup>+</sup>  
534 cells outside the VZ was observed but this was not significantly different from WT (Figure 2  
535 C, D). This suggests that in the *Eml1* cKO, more RG delaminate at early, relative to mid-  
536 corticogenesis.

537 Based on the progenitor abnormalities detected, we decided to investigate if progenitors  
538 exhibit cell cycle defects in the absence of *Eml1*.

### 539 ***Eml1* cKO induces stage-specific cell cycle alterations in VZ RG at** 540 **E12 and E15**

541 We first investigated cell cycle using a method of staggered injection of dual thymidine  
542 analogs in pregnant females at E12.5 and E15.5 (adapted from Harris et al. (Harris et al.,  
543 2018) and schematized in Figure 3 A). Briefly, EdU<sup>+</sup>, BrdU<sup>+</sup>, and Edu+BrdU<sup>+</sup> cells (labeled  
544 with red, green, and white fluorescence) were counted, allowing a calculation of S-phase and  
545 cell cycle length for apical RG (Pax6<sup>+</sup>) (Martynoga et al., 2005; Nowakowski et al., 1989).

546 S-phase duration was increased in *Eml1* cKO RG at E12.5 compared to WT (4.98 h in WT; 9  
547 h in cKO) (Figure 3 B, C, G). The cell cycle duration was also lengthened (8.716 h in WT; 15  
548 h in *Eml1* cKO). G1+G2+M duration was not significantly different, although there was a  
549 tendency for a longer duration in cKO cells (Figure 3 C). We also looked at the distribution of  
550 the cells in S-phase by dividing the cortical wall into 6 identical bins. In the *Eml1* cKO

551 cortical wall, there was an increased proportion of cells entering in S-phase apically (e.g. bin  
552 2) and an inversed tendency for those exiting (Figure 3 D).

553 At E15.5 the cell cycle duration was calculated for *Eml1* cKO RG in the VZ, *Eml1* cKO RG  
554 outside the VZ (ectopic RG), compared to WT RG in the VZ. The total cell cycle duration  
555 was shorter in *Eml1* cKO RG in the VZ (20.67 h in WT; 11.05 h in VZ cKO RG and 15.99 h  
556 in basal ectopic cKO RG) associated with a shortening of G1+G2+M phase (Figure 3 E-G). S-  
557 phase length was not altered significantly at this time point. *Eml1* cKO RG outside the VZ  
558 exhibited an intermediate phenotype between WT and *Eml1* cKO RG in the VZ (Figure 3 E-  
559 G). Cell cycle phase and length durations did not differ significantly from the WT, nor from  
560 cKO RG in the VZ.

561 With the dual injection method, it was not possible to determine the duration for G1 and  
562 G2/M separately, so we additionally performed co-immunolabelling of Ki67 and PCNA,  
563 associating cells to a cell cycle phase based on their labelling pattern (protocol adapted from  
564 Fousse et al. (Fousse et al., 2019), Supplementary Figure 2 A). At E12.5, the proportion of S  
565 phase cells was greater in *Eml1* cKO RG, indicating that the relative duration of S-phase is  
566 longer, as also shown with the dual injection method (Supplementary Figure 2 B, C). At  
567 E15.5, in *Eml1* cKO cells in the VZ, the S-phase proportion of cells was unchanged compared  
568 to WT, whereas G1 phase cells were reduced, and G2/M cells were increased, suggesting a  
569 relative lengthening of G2/M and shortening of G1 duration. Ectopic RG showed no  
570 significant differences compared to WT (Supplementary Figure 2 D, E). Thus, there is overlap  
571 between the results of the two methods, revealing robust defects in S-phase at E12.5, and  
572 pinpointing alterations in G1, G2/M in *Eml1* cKO RG in the VZ at E15.5. In the absence of  
573 *Eml1*, it is clear that progenitors exhibit stage-specific cell cycle alterations. Based on these  
574 and the PC results, we were interested in assessing the possible upstream subcellular and  
575 molecular mechanisms that might help explain the defects.

## 576 ***Eml1* interactome indicates cell cycle and microtubule proteins**

577 To gain insight into potential perturbations of protein interactions that occur when EML1 is  
578 mutated (SH mutation EML1\*T243A (Kielar et al., 2014)), BioID proximity labeling was  
579 performed. BioID uses an abortive *E.coli* biotin ligase (BirA) fused to a target protein to  
580 biotinylate its nearby interactors (Roux et al., 2012). Here, BirA was fused to the N-terminus  
581 of EML1 and EML1\*T243A and expressed in Neuro2A cells. We carefully checked for  
582 centrosomal defects in transfected cells (in interphase and during mitosis), without identifying

583 any obvious abnormalities (Supplementary Figure 3 A). Cell size and multi-nucleation defects  
584 were also not observed.

585 After isolation of biotinylated proteins and tryptic digestion (Figure 4 A), peptides were  
586 analyzed by LC-MS/MS. A SAINT (Significance Analysis of INTeractome) probability (SP)  
587 score (Teo et al., 2014) and fold changes were generated. Using an SP score  $\geq 0.6$  resulted in  
588 49 and 30 proximal interactor proteins for EML1 and EML1\*T243A respectively (Figure 4 B,  
589 C). Thus, the EML1\*T243A interactome comprised fewer proteins compared with the WT.  
590 Also, when 26 common interactors for EML1 and EML1\*T243A were plotted according to  
591 their SP scores (not necessarily falling below  $SP < 0.6$ ), these were found reduced in the  
592 mutant (Figure 4 D). Gene ontology (GO) analyses were performed based on molecular  
593 function, cellular compartment and biological process (Figure 4 E and Supplementary Figure  
594 3 B, C). This showed that the most enriched biological processes are organelle organization,  
595 translation, peptide biosynthetic process, peptide metabolic process, cell cycle and MT-based  
596 processes (Figure 4 E). The GO analyses related to the SH-associated mutant form of EML1  
597 reveal correspondingly fewer of these biological processes. Cross-referencing the BioID hits  
598 showed that a number were also uncovered previously (e.g. (Cep170, Eml4, Dnmt1, Dhx15,  
599 Ddx3x, Nat10, Ddx6, Ruvb1, Eif2s3x, Rpl10a, Tjp1, Dnajc7 and Rpl10) (Bizzotto et al.,  
600 2017).

601 To further investigate the BioID hits of EML1, cellular components related to the  
602 cytoskeleton, spindle and organelles were highlighted (Figure 4 F). Validating the BioID  
603 screen, we were able to co-immunoprecipitate EML1 with EML4 (Supplementary Figure 3  
604 D). Also, Vcpip1 is a previously established WT Eml1 partner, for which the interaction is  
605 lost with the missense mutation (Uzquiano et al., 2019). A further interacting protein that was  
606 specifically identified with WT EML1 is Cep170. This was not identified when EML1 carried  
607 the patient mutation (T243A). Cep170 is known to be essential for centrosome maturation and  
608 is a marker of the mature centriole. We checked for Cep170 intensity at the centrosomes  
609 located at the ventricular surface of E12.5 and E15.5 WT and cKO embryonic brains and  
610 observed that its intensity was significantly decreased in the *Eml1* cKO at E12.5, with a  
611 possible tendency for reduction at E15.5 (Figure 4 G-J, Supplementary Figure 3 E). Eml1  
612 interaction with Cep170 may thus be important for the localization of the latter to  
613 centrosomes. Eml1 could be essential for centrosome integrity during early cortical  
614 development, influencing cell cycle and PC.

615 **Human and mouse centrosomes are defective upon *EML1/Eml1***  
616 **mutation and this is rescued by EpoD treatment**

617 Along with centrosomal and PC proteins identified by BioID (e.g. Cep170, Ckap2, Cct2,  
618 Cct28), several proteins related to the Golgi apparatus were also identified (e.g. Copg2 and  
619 Vcpip1). General secretory trafficking from the Golgi apparatus was indeed shown to be  
620 delayed in *Eml1* mutant RG ((Uzquiano et al., 2019) and data not shown). Cargo trafficking  
621 and Golgi-derived protein transport are key to PC formation, we therefore decided to  
622 investigate PC protein trafficking. Using primary cultures of Pax6+ cells (Sun et al., 2011),  
623 we first tested the Retention Using Selective Hook (RUSH) approach (Boncompain et al.,  
624 2012). Proteins are released from the endoplasmic reticulum (ER)/Golgi after addition of  
625 biotin, and can be monitored in fixed cells at different time points (0, 30, 60 and 90 min, as  
626 schematized in Supplementary Figure 4 A). By performing immuno-labelling of GM130 to  
627 visualize the Golgi (Nakamura et al., 1995) and Arl13b to label the PC, we assessed the  
628 concentration of SSTR3 and PKD2 PC proteins in each organelle over time. In control cells,  
629 we observed that SSTR3-GFP increased in the Golgi at 30 min and in the PC at 60 min  
630 (Supplementary Figure 4 B, C). In *Eml1* cKO progenitors compared to WT, SSTR3-GFP  
631 levels were lower both in the Golgi at 30 min and in the PC at 60 min (Supplementary Figure  
632 4 B, C). For PKD2-GFP, under control conditions, we observed a small increase at the Golgi  
633 at 30 min and in the PC at 60 min, but in *Eml1* cKO a significant increase of the protein was  
634 still observed at the Golgi at 60 min with a tendency for decrease at the PC (Supplementary  
635 Figure 4 D). These abnormal profiles suggest that the anterograde trafficking of PC proteins is  
636 impaired.

637 The centrosome serves as the base of the PC and plays a role in assembly, maintenance and  
638 signaling pathways. Dysfunction of the centrosome can contribute to defects in PC formation  
639 and function, resulting in a variety of diseases, including ciliopathies. Understanding the  
640 relationship between the centrosome and PC is thus important for uncovering the molecular  
641 mechanisms underlying cilia-related dysfunctions. Centrosome structure was hence assessed  
642 using electron microscopy (EM) in human cells from 2 EML1 patients (patient 1, compound  
643 heterozygous, R138X, T243A; patient 2, homozygous, W225R (Jabali et al., 2022)). In cortical  
644 progenitors derived from induced pluripotent stem cells (IPSCs (Jabali et al., 2022)), all  
645 patient cells examined exhibited abnormal centrosomes with poorly formed MT triplets  
646 (Figure 5 A, B). In addition, 83.33% showed MT aggregates near the centrosomes, suggesting

647 centriole assembly defects in patient cells (Figure 5 A, B). Treatment with Etoposide  
648 (EpoD, a microtubule polymerizing and stabilizing agent) was shown previously to rescue PC  
649 length defects in *EML1* patient cells (Jabali et al. 2022). We therefore asked whether this  
650 treatment could also rescue centrosome defects. After EpoD treatment, 86% of EML1 patient  
651 cells showed rescued centrosomal structure and fewer cells (37.93%) showed MT aggregates  
652 in the vicinity of the centrosomes (Figure 5 A, B). These results may indicate that centrosome  
653 defects contribute to PC formation defects in mutant cells.

654 Given these results, key centrosome proteins were assessed in primary cultures of Pax6+ cells  
655 from *Eml1* cKO mouse brain. Labeling for  $\gamma$ -tubulin (a marker of centrosomes) showed that  
656 the number of  $\gamma$ -tubulin puncta per cell was not altered significantly in mutant cells however  
657 the intensity of  $\gamma$ -tubulin was decreased (Figure 5 C, D). Also, pericentrin (pcnt), a marker of  
658 pericentriolar material (PCM), a complex of proteins surrounding centrioles, was reduced in  
659 intensity (Figure 5 C, E). The relative dispersion of the PCM, measured from the pcnt-labelled  
660 area, may also be decreased (Figure 5 E). Thus, *EML1/ Eml1* seems to contribute to  
661 centrosome integrity in human and in mouse progenitors.

## 662 ***Eml1* is essential for the recruitment of key proteins at the** 663 **centrosome**

664 To detect centrosomes *in vivo* during early and mid-corticogenesis,  $\gamma$ -tubulin and pcnt were  
665 examined in coronal brain sections. The distribution of centrosomes along the cortical wall at  
666 E12.5 and E15.5 was revealed by labelling with  $\gamma$ -tubulin. At E12.5, mutant brain  
667 centrosomes were abnormally distributed with fewer  $\gamma$ -tubulin (+) puncta in the first 10  $\mu$ m  
668 above the ventricular surface and more within the 10 - 20  $\mu$ m range compared to WT (Figure  
669 6 A, B). A similar trend was observed at E15.5 (Figure 6 D, E). This suggests that centrosome  
670 distribution may be altered prior to the observation of detached RG. Overall numbers of  
671 puncta at each stage are unchanged (Supplementary Figure 5 A). We also checked for  $\gamma$ -  
672 tubulin intensity at the ventricular surface and observed at E12.5 a tendency for decreased  
673 fluorescence intensity in *Eml1* cKO conditions, with fewer obvious changes at E15.5 (Figure  
674 6 C, F; Supplementary Figure 5 B). Likewise, labelling for pcnt revealed that PCM dispersion  
675 was reduced in the cKO condition specifically at E12.5, but not at E15.5 (Figure 6 G, H;  
676 Supplementary Figure 5 C). These results suggest that at E12.5,  $\gamma$ -tubulin and pcnt are not  
677 well recruited to the centrosomes in the absence of *Eml1*.



## 678 **Microtubule growth is reduced in the absence of Eml1**

679 The centrioles and the PCM contain proteins that nucleate and stabilize MTs. Indeed,  
680 centrioles act as templates for the formation of MTs that grow outward from the centrosome,  
681 providing the cell with a polarized cytoskeleton. Since we observed PC and centrosomal  
682 defects in Eml1 deficient cortical cells, we also tested how possible reduced protein  
683 complexes at the MTOC might alter MT nucleation activity. In Pax6<sup>+</sup> cells in culture, MT  
684 regrowth was studied at 1 and 2 minutes after MT depolymerization, showing robust growth  
685 in WT around pericentrin<sup>+</sup> puncta (Figure 7 A, B). In *Eml1* mutant cells, less puncta were  
686 associated with MT regrowth (Figure 7 A, B). Among MTs surrounding centrosomes, their  
687 average length appeared unaffected (Figure 7 C).

688 We next assessed MTs in brain tissue with  $\alpha$ -tubulin labeling in coronal sections of E12.5  
689 embryonic brains. In the VZ, assessing the distribution of fluorescence intensity from the  
690 ventricular surface to a height of 100- $\mu$ m in the WT VZ, an enrichment of  $\alpha$ -tubulin was  
691 observed at the apical surface, however this was greatly reduced in the *Eml1* cKO  
692 (Supplementary Figure 5 D, E). There was also a tendency for decreased  $\alpha$ -tubulin  
693 fluorescence intensity in the absence of Eml1 (Supplementary Figure 5 D, F).

694 These combined results suggest that centrosome phenotypes, including in the VZ, may  
695 influence efficient MT formation, potentially impacting RG behavior.

## 696 **RG detachment is partially rescued with EpoD treatment in vivo**

697 Because EpoD treatment rescues centrosome and PC defects, we tested if this treatment could  
698 also rescue RG detachment *in vivo*. To do so, we injected EpoD intraperitoneally into  
699 pregnant females consecutively at E11.5 and E12.5 and sacrificed them at E13.5. Pax6  
700 immunolabelling was then performed in embryonic brain slices, and results were compared  
701 with saline-injected embryos. Cortical wall and VZ thickness were compared and no  
702 significant differences were found for these parameters (Figure 8 A, B), nor for overall cell  
703 number in the VZ, although there was a possible tendency for reduction in the cKO (upon  
704 EpoD treatment  $114.08 \pm 3.02$  Hoechst labeled cells per ROI in control versus  $104.42 \pm 3.86$  in  
705 *Eml1* cKO). The proportion of detached Pax6<sup>+</sup> cells in the *Eml1* cKO in both saline and  
706 EpoD conditions was still increased, however with the EpoD treatment, detachment was  
707 significantly less than in saline conditions (Figure 8 C, right). Of note, the number of Pax6(+)  
708 cells in the *Eml1* cKO is increased under saline conditions compared to the WT but this is no

709 longer the case after EpoD treatment (Figure 8 C, left), suggesting that the increased number  
710 of Pax6+ cells may be linked to increased detached RG. Further verifying the cells outside the  
711 VZ, shows in the cKO that 60 % of cells are Pax6+ve in the cKO at this age under saline  
712 conditions and is reduced to 32% upon EpoD treatment. Verifying the number of Pax6  
713 negative cells outside the VZ, although the results were not significant between the  
714 conditions, a tendency for reduction in the cKO was observed compared to control under  
715 saline conditions and the trend remains the same upon EpoD treatment (133.33±8.99 per ROI  
716 in control vs 101.5±7.11 in *Eml1* cKO under saline conditions and 122.92±13.88 in control vs  
717 103.33±13.33 in *Eml1* cKO under EpoD treatment). We hence do not rule out that  
718 neurogenesis is slightly reduced at this timepoint in the cKO.

719 To further analyze the effects of EpoD on heterotopia formation subsequent to RG  
720 detachment, we allowed the embryos to develop until E18.5 after being treated either by  
721 saline or EpoD consecutively at E11.5 and E12.5. Whole embryonic brains were stained for  
722 SatB2 and subsequently cleared for 3D imaging. As *Satb2*+ neurons form a compact layer of  
723 cells covering the whole surface of the heterotopia, we used this staining to delineate the  
724 shape of the malformation (Figure 8 D). The volume of the heterotopia was thus quantified  
725 and normalized to the corresponding homotopic cortex. Our results suggest that EpoD  
726 treatment in early corticogenesis partially reduces the volume of the heterotopia at E18.5  
727 (Figure 8 E). *Satb2* mean fluorescent intensities did not appear to change between conditions  
728 (Figure 8 F). Thus, we pinpoint early MT-dependent defects in the *Eml1* cKO that influence  
729 both apical RG attachment and heterotopia formation.

730

## 731 **Discussion**

732 With this study we pinpoint early roles for *Eml1* in cortical development by analyzing the  
733 phenotypes occurring before the heterotopia arises in a dorsal telencephalon-specific cKO.  
734 Specifically, we identified that 1) RG start to delaminate after E12.5; 2) there are cell cycle  
735 modifications which differ across the developmental window starting from this time point; 3)  
736 *Eml1* is central for the centrosome function and 4) transient microtubule stabilization at early  
737 stages partially rescues the *Eml1* cKO defects. Altogether these novel results raise several  
738 intriguing questions.

739 RG detachment preferentially occurs at early but not mid-corticogenesis suggesting that there  
740 may be a critical time window in the *Eml1* cKO mouse to produce ectopic RG. Thus, the early

741 defects we detected are likely to be correlated with detachment. We checked if *Eml1*  
742 expression from E12.5 to E15.5 varies, using the humous.org database (Klingler et al., 2021),  
743 and observed that in mouse, the expression of *Eml1* does not vary, but in Human it is enriched  
744 at early corticogenesis compared to mid-corticogenesis in RG. To further understand mouse  
745 developmental stage progenitor differences, and focusing on the specific alteration of  $\gamma$ -  
746 tubulin, *pcnt* and their defects at the centrosomes, we analyzed expression in WT apical  
747 progenitors using RNA sequencing data from Telley and colleagues (Telley et al., 2019).  
748 Expression of *pcnt*, and  $\gamma$ -tubulin are reduced from E12.5 to E15.5 in mouse, suggesting that  
749 they could be more important in early than late stages. Cortical progenitors were shown to  
750 have different features at specific stages (Telley et al., 2019) so it is expected that they change  
751 over time. Centrosomal protein composition also varies along corticogenesis and  
752 differentiation (O'Neill et al., 2022). Our work hence further underlines that centrosome  
753 function could be critical at certain stages. These combined data may help explain specific  
754 defects occurring in particular time-windows, compatible with the deregulated processes we  
755 identify. It is also of interest to note that basal RG (bRG) formation in gyrencephalic species  
756 also may occur in a defined period. In ferret for example, it has been shown that there is a  
757 peak of bRG production between E30 to E34 (Martínez-Martínez et al., 2016). This process  
758 may share common features with *Eml1* mutant results.

759 We also show distinct cell cycle alterations at early and mid-corticogenesis. S-phase  
760 lengthening was observed in E12.5 *Eml1* cKO RG, which may be correlated with a more  
761 proliferative behavior of these cells. Indeed, it has been shown that RG with a longer S-phase  
762 are prone to be more proliferative (Arai et al., 2011). Coherent with this, we found more  
763 Pax6<sup>+</sup> cells in total at E13.5 but not at E12.5, suggesting an amplification of the Pax6<sup>+</sup> cell  
764 pool. Of note, we also observe that, while Pax6<sup>+</sup> cells increase significantly starting from  
765 E13.5, the VZ thickness does not decrease until E14.5/E15.5. It is possible that Pax6<sup>+</sup> cells  
766 outside the VZ are the product of already detached and proliferating Pax6<sup>+</sup> cells, and not  
767 simply those directly detached from the VZ. However, in *EML1*-mutant organoids, it was  
768 shown that Pax6<sup>+</sup> cells in the VZ-like niche exhibited increased nuclear YAP1, a downstream  
769 effector of HIPPO signaling linked with proliferation and S-phase entry (Jabali et al., 2022).  
770 Pharmacological inhibition of YAP1 significantly reduced the numbers of ectopic neural  
771 rosettes in *EML1*-mutant organoids (Jabali et al., 2022). Also, positive regulators of  
772 proliferation are increased at the transcriptional level in *EML1* mutant organoids. Other works  
773 show that, especially during S phase, centrosomes can have an MT-independent role. For

774 instance, targeting of polo kinase 1 (Plk1) to the centrosomes or  $\gamma$ -tubulin subcellular  
775 localization are both essential for S-phase progression (Shen et al., 2013). Thus, there may be  
776 several reasons for S-phase lengthening.

777 At later stages, we observed cell cycle duration shortening in the VZ, a decreased number of  
778 cells in G1 phase and increased numbers in G2/M. At E15.5, there are less cells in the VZ  
779 leading to its thinning. We can imagine that INM distance is shortened, and thus perhaps cells  
780 can advance faster through the cell cycle. It has also already been observed that recombinant  
781 Eml1 can localize to the mitotic spindle (Kielar et al., 2014) which may help explain in its  
782 absence, why there might be a longer G2/M in mutant cells, although it is unclear why this  
783 might specifically affect later stages. Moreover, at E15.5 we observe that ectopic versus VZ  
784 RG are not equally affected in terms of cell cycle. It is indeed known that human bRG are  
785 subject to a different environment compared to RG in the VZ, and they locally produce  
786 growth factors such as PDGFD (Lui et al., 2014), and require a modified extracellular matrix  
787 (ECM), in terms of components and receptors, that play crucial role in neuronal progenitor  
788 proliferation and behaviour (Ferent et al., 2020). Furthermore, bRG have less contact with the  
789 embryonic cerebrospinal fluid (eCSF) and hence less exposure to its secreted factors with an  
790 impact on signaling. These elements might help explain the differences between the two  
791 populations. Concerning the neuronal output of altered VZ progenitors, these increased cells  
792 might collectively increase the number of neurons at a later timepoint; on the other hand, VZ  
793 cells at E15.5 may also individually produce less neurons, as they have a shorter G1  
794 (Takahashi et al., 1995). VZ cell composition may differ in the mutant, potentially containing  
795 a higher proportion of Pax6-negative cells than in controls, although this remains to be  
796 examined.

797 Because of the central role of the centrosome and PC in proliferation, we investigated protein  
798 trafficking to these organelles. Regarding the diversity of possible routes taken by ciliary  
799 proteins to reach the PC (Long & Huang, 2020), we do not yet know which of those may be  
800 exclusively or partially altered in *Eml1* mutant conditions. Recently, it was shown in RG, that  
801 post-Golgi apical trafficking occurs in the direction of the MT minus ends, via the Rab6-  
802 dynein-Lis1 complex, which is required for apical localization of Crumbs3 (Brault et al.,  
803 2022), a major apical domain determinant (Bulgakova & Knust, 2009). Therefore, genetic  
804 inactivation of Rab6A/B or Lis1 induces a retraction of the RG apical process, leading to  
805 delamination and ectopic division (Brault et al., 2022). Thus, known apical trafficking defects  
806 to regions of the cell containing the centrosome and PC strongly resemble the *Eml1* cKO

807 phenotype. For example, Eml1 interacts with the GA protein Vcpip1, and its interaction is  
808 reduced when Eml1 has the T234A patient mutation ((Uzquiano et al., 2019) and our BioID  
809 data). Also, GA morphological defects were found in human and mouse cells in *EML1/Eml1*  
810 mutant conditions (Uzquiano et al., 2019), suggesting that ciliary routes from this organelle  
811 could be impaired. Indeed, increased accumulation of PKD2 in the GA in RUSH experiments  
812 suggest a GA trafficking defect. SSTR3, for which we found decreased protein in the GA as  
813 well as the PC, may exhibit an ER-GA protein transport alteration in the mutant. Recombinant  
814 EML1 exhibits a vesicular pattern on MTs, altered with T243A mutation (Kielar et al., 2014).  
815 We can hypothesize that through its ability to bind MTs, Eml1 can influence MT integrity and  
816 the trafficking of cargos including PC proteins. Eml1 can also influence centrosome MT  
817 integrity.

818 It is known that mutations of genes coding for tubulin proteins are associated with cortical  
819 malformations (Poirier et al., 2013). Here, we showed that during early cortical development,  
820 MTs are defective at the apical surface, and MT re-growth is impaired in Pax6+ cells in  
821 culture. It was recently shown that EML1 is involved in MT nucleation as well as associating  
822 strongly with growing MTs, with a unique pattern of accumulation towards their ends  
823 (Jijumon et al., 2022). Patient mutations alter this co-localization with MTs, quite possibly  
824 impacting MT dynamics and architecture. MT stabilization with EpoD rescues centrosomal  
825 defects in human patient cells. EpoD treatment also partially rescued RG detachment in the  
826 *Eml1* cKO, underlining an involvement of MT-dependent mechanisms in pathogenic  
827 detachment. EpoD's effect may be by stabilization of centrosomes and nucleated MTs, even  
828 though the latter may be fewer in number in the cKO. We showed that EpoD injections in  
829 early corticogenesis not only partially rescues RG detachment at E13.5, but remarkably, can  
830 also reduce the volume of heterotopia several days later at E18.5. It would be interesting to  
831 assess if EpoD treatment rescues cell cycle parameters as well, in order to determine their link  
832 to MT defects, and the extent to which cell cycle alterations are involved in RG detachment.  
833 Further in-depth studies will address this, as our transient, early EpoD treatment clearly  
834 targets an important time window for RG manipulation. These promising results in a  
835 preclinical mouse model of heterotopia may help pinpoint future pertinent interventions for  
836 this severe disorder.

## 837 **Data availability**

838 The mass spectrometry proteomics data (BioID) have been deposited to the ProteomeXchange  
839 Consortium via the PRIDE partner repository (<https://www.ebi.ac.uk/pride/>) with the dataset

840 identifier PXD045846. The main body of data (including images and analyses) are available  
841 in the article or online supplemental material. Source data are provided with this paper for  
842 Western blots. All other source data are available from the authors upon reasonable request.

## 843 **Acknowledgements**

844 We are grateful to Dr. A. Baffet, V. Marthiens and members of the lab for comments and  
845 discussions. We thank Dominic Norris for the RUSH PKD2 construction and Gaëlle  
846 Boncompain for aid with other RUSH constructs. We thank Anne Houllier for aid with  
847 Western blots and lab members for support. We thank the IFM animal experimentation  
848 facility, and cellular and tissue imaging platforms at the Institut du Fer à Moulin, supported  
849 also by the Région Ile de France and the FRC Rotary.

850 This project was supported by the French ANR under the frame of E-Rare-3, the ERA-Net for  
851 Research on Rare Diseases (ERARE18-049, to F.F., D.J, & N.O.) and the Fondation pour la  
852 recherche medicale (FRM, Equipe FRM 2020 awarded to F.F. EQU202003010323). Further  
853 funding was obtained from the JTC 2015 Neurodevelopmental Disorders affiliated with the  
854 ANR (for NEURON8-Full- 815-006 STEM-MCD, to F.F and JL) and the Hector Stiftung II  
855 and the German research foundation (DFG) project LA 2933/2-1 to JL). F.F.'s group were  
856 also involved in the European Cooperation on Science and Technology (COST Action  
857 CA16118), NeuroMIG project. F.F.'s lab was previously associated with the BioPsy Labex  
858 project and the Ecole des Neurosciences de Paris Ile-de-France (ENP) network. Our salaries  
859 and lab were supported by Inserm and the Centre national de la recherche scientifique  
860 (CNRS). D.Z. was supported by an FRM grant FDT202204015115 and Sorbonne University.  
861 K.C was supported by a Bourse Valérie Chamillard awarded by the Fondation de France  
862 after ranking by the French Foundation for Research on Epilepsy. V.V. was supported by  
863 Sorbonne University. J.F. obtained funding from the ATIP-Avenir program. The ANR project  
864 Ribocortex helped support this project (ANR-22-CE16-0025-01).

## 865 **Conflicts of interest**

866 The authors declare no competing financial interests.

## 867 **Contributions**

868 Donia Zaidi: conceptualization, investigation, formal analysis, validation, visualization,  
869 methodology, supervision for animal and in vitro experiments, as well as writing (original

870 draft as well as review and editing). Kaviya Chinnappa: investigation, formal analysis,  
871 validation, methodology for animal experiments, especially in utero electroporation, as well  
872 as writing (original draft as well as review and editing). Valeria Viola: investigation, formal  
873 analysis, validation, for animal experiments, as well as writing (original draft as well as  
874 review and editing). Berfu Nur-Yigit: investigation, formal analysis, visualization and  
875 validation for BioID experiments, as well as writing (original draft as well as review and  
876 editing). Nurhan Ozlu: conceptualization, project administration, funding acquisition,  
877 methodology, investigation, formal analysis, supervision, visualization and validation for  
878 BioID experiments, as well as writing (original draft as well as review and editing). Carmen  
879 Cifuentes-Diaz: investigation, formal analysis, validation, visualization for performing EM  
880 experiments., and writing (original draft as well as review and editing). Julien Ferent: formal  
881 analysis, funding acquisition, investigation, methodology, supervision, validation and  
882 visualization for model characterization and 3D heterotopia data, as well as writing (original  
883 draft as well as review and editing). Ana Uzquiano: investigation, formal analysis,  
884 visualization, methodology, supervision for animal and in vitro experiments, and writing  
885 (original draft as well as review and editing). Ammar Jabali: investigation, formal analysis,  
886 validation, methodology, for human in vitro experiments, and writing of the original draft.  
887 Julia Ladewig: formal analysis, funding acquisition, investigation, methodology, supervision,  
888 validation and visualization for human in vitro work, as well as writing (original draft as well  
889 as review and editing). Emilie Lemesre: methodology and resources generating and supplying  
890 RUSH constructs. Franck Perez: methodology and supervision for generating and supplying  
891 RUSH constructs, validation and visualization. Fiona Francis: project administration, funding  
892 acquisition, conceptualization, investigation, formal analysis, validation, visualization,  
893 methodology and supervision, as well as writing (original draft as well as review and editing).

## 894 **Supplementary material**

895

896 Supplementary material is available at *JCB* online.

897

## 898 **References**

- 899 1. Götz M, Barde YA. Radial glial cells: Defined and major intermediates between  
900 embryonicstem cells and CNS neurons. Vol. 46, Neuron. 2005.

- 901 2. Noctor SC, Flint AC, Weissman TA, Dammerman RS, Kriegstein AR. Neurons  
902 derived from radial glial cells establish radial units in neocortex. *Nature*.  
903 2001;409(6821):714–20.
- 904 3. Noctor SC, Martinez-Cerdeño V, Ivic L, Kriegstein AR. Cortical neurons arise in  
905 symmetric and asymmetric division zones and migrate through specific phases. *Nat*  
906 *Neurosci*. 2004;7(2).
- 907 4. Rakic P. Mode of cell migration to the superficial layers of fetal monkey neocortex. *J*  
908 *Comp Neurol J Comp Neurol*. 1972;145(1):61–83.
- 909 5. Sauer ME, Walker BE. Radioautographic Study of Interkinetic Nuclear Migration in  
910 the Neural Tube. *Proc Soc Exp Biol Med*. 1959;101(3).
- 911 6. Spear PC, Erickson CA. Interkinetic nuclear migration: A mysterious process in search  
912 of a function. Vol. 54, *Development Growth and Differentiation*. 2012.
- 913 7. Tsai JW, Lian WN, Kemal S, Kriegstein AR, Vallee RB. Kinesin 3 and cytoplasmic  
914 dynein mediate interkinetic nuclear migration in neural stem cells. *Nat Neurosci*.  
915 2010;13(12).
- 916 8. Stouffer MA, Golden JA, Francis F. Neuronal migration disorders: Focus on the  
917 cytoskeleton and epilepsy. *Neurobiol Dis*. 2016;92(Part A).
- 918 9. Romero DM, Bahi-Buisson N, Francis F. Genetics and mechanisms leading to human  
919 cortical malformations. Vol. 76, *Seminars in Cell and Developmental Biology*. 2018.
- 920 10. Kielar M, Tuy FPD, Bizzotto S, Lebrand C, De Juan Romero C, Poirier K, et al.  
921 Mutations in *Eml1* lead to ectopic progenitors and neuronal heterotopia in mouse and  
922 human. *Nat Neurosci*. 2014;17(7).
- 923 11. Shaheen R, Sebai MA, Patel N, Ewida N, Kurdi W, Altweijri I, et al. The genetic  
924 landscape of familial congenital hydrocephalus. *Ann Neurol*. 2017;81(6).
- 925 12. Markus F, Kannengießer A, Näder P, Atigbire P, Scholten A, Vössing C, et al. A novel  
926 missense variant in the *EML1* gene associated with bilateral ribbon-like subcortical  
927 heterotopia leads to ciliary defects. *J Hum Genet*. 2021;66(12).
- 928 13. Oegema R, McGillivray G, Leventer R, Le Moing AG, Bahi-Buisson N, Barnicoat A,  
929 et al. *EML1*-associated brain overgrowth syndrome with ribbon-like heterotopia. Vol.



- 930 181, American Journal of Medical Genetics, Part C: Seminars in Medical Genetics.  
931 2019.
- 932 14. Bizzotto S, Francist F. Morphological and functional aspects of progenitors perturbed  
933 in cortical malformations. Vol. 9, *Frontiers in Cellular Neuroscience*. 2015.
- 934 15. Collins SC, Uzquiano A, Selloum M, Wendling O, Gaborit M, Osipenko M, et al. The  
935 neuroanatomy of Eml1 knockout mice, a model of subcortical heterotopia. *J Anat*.  
936 2019;235(3).
- 937 16. Grosenbaugh DK, Joshi S, Fitzgerald MP, Lee KS, Wagley PK, Koepfel AF, et al. A  
938 deletion in Eml1 leads to bilateral subcortical heterotopia in the tish rat. *Neurobiol Dis*.  
939 2020;140.
- 940 17. Uzquiano A, Cifuentes-Diaz C, Jabali A, Romero DM, Houllier A, Dingli F, et al.  
941 Mutations in the Heterotopia Gene Eml1/EML1 Severely Disrupt the Formation of  
942 Primary Cilia. *Cell Rep*. 2019;28(6).
- 943 18. Richards MW, O'Regan L, Roth D, Montgomery JM, Straube A, Fry AM, et al.  
944 Microtubule association of EML proteins and the EML4-ALK variant 3 oncoprotein  
945 require an N-terminal trimerization domain. *Biochem J*. 2015;467(3).
- 946 19. Borrell V, Götz M. Role of radial glial cells in cerebral cortex folding. Vol. 27, *Current*  
947 *Opinion in Neurobiology*. 2014.
- 948 20. Penisson M, Ladewig J, Belvindrah R, Francis F. Genes and Mechanisms Involved in  
949 the Generation and Amplification of Basal Radial Glial Cells. 2019;13(August):1–21.
- 950 21. Bizzotto S, Uzquiano A, Dingli F, Ershov D, Houllier A, Arras G, et al. Eml1 loss  
951 impairs apical progenitor spindle length and soma shape in the developing cerebral  
952 cortex. *Sci Rep*. 2017;7(1).
- 953 22. Jabali A, Hoffrichter A, Uzquiano A, Marsoner F, Wilkens R, Siekmann M, et al.  
954 Human cerebral organoids reveal progenitor pathology in EML1-linked cortical  
955 malformation. *EMBO Rep*. 2022
- 956 23. Gorski JA, Talley T, Qiu M, Puelles L, Rubenstein JLR, Jones KR. Cortical excitatory  
957 neurons and glia, but not GABAergic neurons, are produced in the Emx1-expressing  
958 lineage. *J Neurosci*. 2002;22(15).

- 959 24. Renier N, Adams EL, Kirst C, Wu Z, Azevedo R, Kohl J, et al. Mapping of Brain  
960 Activity by Automated Volume Analysis of Immediate Early Genes. *Cell*. 2016;165(7).
- 961 25. Sun T, Wang XJ, Xie SS, Zhang DL, Wang XP, Li BQ, et al. A comparison of  
962 proliferative capacity and passing potential between neural stem and progenitor cells  
963 in adherent and neurosphere cultures. *Int J Dev Neurosci*. 2011;29(7).
- 964 26. Boncompain G, Divoux S, Gareil N, De Forges H, Lescure A, Latreche L, et al.  
965 Synchronization of secretory protein traffic in populations of cells. *Nat Methods*.  
966 2012;9(5).
- 967 27. Boncompain G, Fourriere L, Gareil N, Perez F. Retention Using Selective Hooks-  
968 Synchronized Secretion to Measure Local Exocytosis. In: *Methods in Molecular*  
969 *Biology*. 2021.
- 970 28. Martynoga B, Morrison H, Price DJ, Mason JO. Foxg1 is required for specification of  
971 ventral telencephalon and region-specific regulation of dorsal telencephalic precursor  
972 proliferation and apoptosis. *Dev Biol*. 2005;283(1).
- 973 29. Harris L, Zalucki O, Piper M. BrdU/EdU dual labeling to determine the cell-cycle  
974 dynamics of defined cellular subpopulations. *J Mol Histol*. 2018;49(3).
- 975 30. Nowakowski RS, Lewin SB, Miller MW. Bromodeoxyuridine immunohistochemical  
976 determination of the lengths of the cell cycle and the DNA-synthetic phase for an  
977 anatomically defined population. *J Neurocytol*. 1989;18(3).
- 978 31. Shibui S, Hoshino T, Vanderlaan M, Gray JW. Double labeling with iodo- and  
979 bromodeoxyuridine for cell kinetics studies. *J Histochem Cytochem [Internet]*.  
980 1989;37(7):1007–11. Available from: <https://doi.org/10.1177/37.7.2659659>
- 981 32. Fousse J, Gautier E, Patti D, Dehay C. Developmental changes in interkinetic nuclear  
982 migration dynamics with respect to cell-cycle progression in the mouse cerebral cortex  
983 ventricular zone. *J Comp Neurol*. 2019;527(10).
- 984 33. Liu X, Salokas K, Weldatsadik RG, Gawriyski L, Varjosalo M. Combined proximity  
985 labeling and affinity purification–mass spectrometry workflow for mapping and  
986 visualizing protein interaction networks. *Nat Protoc*. 2020;15(10).
- 987 34. Teo G, Liu G, Zhang J, Nesvizhskii AI, Gingras AC, Choi H. SAINTexpress:  
988 Improvements and additional features in Significance Analysis of INTeractome

- 989 software. *J Proteomics*. 2014;100.
- 990 35. Szklarczyk D, Gable AL, Nastou KC, Lyon D, Kirsch R, Pyysalo S, et al. The STRING  
991 database in 2021: Customizable protein-protein networks, and functional  
992 characterization of user-uploaded gene/measurement sets. *Nucleic Acids Res*.  
993 2021;49(D1).
- 994 36. Raudvere U, Kolberg L, Kuzmin I, Arak T, Adler P, Peterson H, et al. G:Profiler: A  
995 web server for functional enrichment analysis and conversions of gene lists (2019  
996 update). *Nucleic Acids Res*. 2019;47(W1).
- 997 37. Shannon P, Markiel A, Ozier O, Baliga NS, Wang JT, Ramage D, et al. Cytoscape: A  
998 software Environment for integrated models of biomolecular interaction networks.  
999 *Genome Res*. 2003;13(11).
- 1000 38. Englund C, Fink A, Lau C, Pham D, Daza RAM, Bulfone A, et al. Pax6, Tbr2, and  
1001 Tbr1 are expressed sequentially by radial glia, intermediate progenitor cells, and  
1002 postmitotic neurons in developing neocortex. *J Neurosci*. 2005;25(1):247–51.
- 1003 39. Roux KJ, Kim DI, Raida M, Burke B. A promiscuous biotin ligase fusion protein  
1004 identifies proximal and interacting proteins in mammalian cells. *J Cell Biol*.  
1005 2012;196(6).
- 1006 40. Nakamura N, Rabouille C, Watson R, Nilsson T, Hui N, Slusarewicz P, et al.  
1007 Characterization of a cis-Golgi matrix protein, GM130. *J Cell Biol*. 1995;131(6 II).
- 1008 41. Telley L, Agirman G, Prados J, Amberg N, Fièvre S, Oberst P, et al. Temporal  
1009 patterning of apical progenitors and their daughter neurons in the developing  
1010 neocortex. *Science* (80- ). 2019;364(6440).
- 1011 42. O’Neill AC, Uzbas F, Antognolli G, Merino F, Draganova K, Jäck A, et al. Spatial  
1012 centrosome proteome of human neural cells uncovers disease-relevant heterogeneity.  
1013 *Science*. 2022 Jun;376(6599):eabf9088.
- 1014 43. Martínez-Martínez MÁ, De Juan Romero C, Fernández V, Cárdenas A, Götz M,  
1015 Borrell V. A restricted period for formation of outer subventricular zone defined by  
1016 *Cdh1* and *Trnp1* levels. *Nat Commun*. 2016;7.
- 1017 44. Arai Y, Pulvers JN, Haffner C, Schilling B, Nüsslein I, Calegari F, et al. Neural stem  
1018 and progenitor cells shorten S-phase on commitment to neuron production. *Nat*

- 1019 Commun. 2011;2(1).
- 1020 45. Shen M, Cai Y, Yang Y, Yan X, Liu X, Zhou T. Centrosomal protein FOR20 is  
1021 essential for S-phase progression by recruiting Plk1 to centrosomes. Cell Res.  
1022 2013;23(11).
- 1023 46. Lui JH, Nowakowski TJ, Pollen AA, Javaherian A, Kriegstein AR, Oldham MC.  
1024 Radial glia require PDGFD-PDGFR $\beta$  signalling in human but not mouse neocortex.  
1025 Nature. 2014;515(7526).
- 1026 47. Ferent J, Zaidi D, Francis F. Extracellular Control of Radial Glia Proliferation and  
1027 Scaffolding During Cortical Development and Pathology. Vol. 8, Frontiers in Cell and  
1028 Developmental Biology. 2020.
- 1029 48. Takahashi T, Nowakowski RS, Caviness VS. The cell cycle of the pseudostratified  
1030 ventricular epithelium of the embryonic murine cerebral wall. J Neurosci. 1995;15(9).
- 1031 49. Long H, Huang K. Transport of Ciliary Membrane Proteins. Vol. 7, Frontiers in Cell  
1032 and Developmental Biology. 2020.
- 1033 50. Brault J, Bardin S, Lampic M, Carpentieri JA, Coquand L, Penisson M, et al. RAB6  
1034 and dynein drive post-Golgi apical transport to prevent neuronal progenitor  
1035 delamination . EMBO Rep. 2022;23(10).
- 1036 51. Bulgakova NA, Knust E. The Crumbs complex: From epithelial-cell polarity to retinal  
1037 degeneration. Vol. 122, Journal of Cell Science. 2009.
- 1038 52. Poirier K, Lebrun N, Broix L, Tian G, Saillour Y, Boscheron C, et al. Mutations in  
1039 TUBG1, DYNC1H1, KIF5C and KIF2A cause malformations of cortical development  
1040 and microcephaly. Nat Genet. 2013;45(6).
- 1041 53. Jijumon AS, Bodakuntla S, Genova M, Bangera M, Sackett V, Besse L, et al. Lysate-  
1042 based pipeline to characterize microtubule-associated proteins uncovers unique  
1043 microtubule behaviours. Nat Cell Biol. 2022;24(2).

1044

## 1045 **Figure legends**

1046 **Figure 1. Pax6<sup>+</sup> cells start to detach during early corticogenesis with PC defects**  
1047 **observed earlier in the *Em11* cKO mouse model. A. Representative images of**

1048 immunolabelling for Pax6 in WT and *Eml1* cKO embryonic brain coronal sections from  
1049 E12.5 to E15.5. **B.** Quantifications of Pax6+ cell counts per region of interest (ROI of 200  $\mu$ m  
1050 width) and **C.** proportion of detached Pax6+ cells above the VZ, expressed as mean +/- SEM.  
1051 **D.** Quantifications of cortical wall thickness (CW), ventricular zone thickness (VZ) and the  
1052 percentage of VZ/CW, represented as mean +/- SEM. Analyses performed at least on 3  
1053 individuals from 2 different litters and 2 sections per individual for each genotype and age. **E.**  
1054 Representative images of immunolabelling for Arl13b at the ventricular surface at E12.5 for  
1055 WT and *Eml1* cKO. **F, G.** Quantification of cilia mean size and number at E12.5, expressed as  
1056 mean +/- SEM. **H, I, J.** Similar analyses performed at E15.5 with 5 individuals per genotype  
1057 and age, analyzed from 3 different litters. Test and significance: Two-way Anova, Sidak's  
1058 multiple comparison (Pax6 analyses, CW and VZ thickness (data distribution was assumed to  
1059 be normal but this was not formally tested)), Mann-Whitney (Arl13b analyses). *P-value* <0.05  
1060 \*, <0.01 \*\*, <0.001 \*\*\*, <0.0001 \*\*\*\*. Scale bars (equivalent for WT and cKO): 30  $\mu$ m in A,  
1061 20  $\mu$ m in E and 10  $\mu$ m in H.

1062

1063 **Figure 2. Abnormal detachment of RG occurs at early but not mid-corticogenesis. A.**  
1064 Representative images and, **B.** Quantification of the distribution of GFP+Pax6+ cells in the  
1065 VZ or outside the VZ between WT and *Eml1* cKO brains one day post-IUE, at E13.5. **C.**  
1066 Representative images and, **D.** Quantification of the distribution of GFP+Pax6+ cells in the  
1067 VZ or outside the VZ between WT and *Eml1* cKO brains one day post-IUE, at E15.5.  
1068 Histograms show mean +/- SEM. Boxes with dotted lines indicate the areas of higher  
1069 magnification images displayed. Arrows indicate GFP+Pax6+ double positive cells. N=5 for  
1070 each condition from 3-4 litters. Test and significance: Two-way Anova, Sidak's multiple  
1071 comparison test. Data passed normality test. *P-value* <0.0001 \*\*\*\*. Scale bars (A,C,  
1072 equivalent for WT and cKO): 50  $\mu$ m (for main and insets).

1073

1074 **Figure 3. Cell cycle analyses of Pax6 (+) cells in E12.5 and E15.5 WT and *Eml1* cKO**  
1075 **brains. A.** Schematic representation of EdU and BrdU injections performed for cell cycle  
1076 analyses and related formulae to calculate duration of S-phase and the cell cycle. **B.**  
1077 Representative images of EdU/BrdU/Pax6 labelling of E12.5 coronal brain slices from WT  
1078 and *Eml1* cKO. **C.** Quantifications of S-phase length (Ts), cell cycle length (Tc), G1+G2+M  
1079 length in hours at E12.5, expressed as mean +/- SEM. **D.** Distribution of cells in the E12.5

1080 cortical wall divided into 6 identical bins. Distributions are shown for cells entering in S-  
1081 phase, maintained in S-phase and for those that exit S-phase, expressed as mean +/- SEM. **E,**  
1082 **F.** Similar analyses performed at E15.5, comparing mutant cells in the VZ and outside. **G.**  
1083 Schematic representation of cell cycle phase lengths for results obtained at E12.5 and E15.5 in  
1084 WT and *Eml1* cKO embryos. Analysis was performed on 5 individuals from 3 litters per  
1085 genotype and 2 ROI were analyzed per individual. Test and significance: Mann-Whitney,  
1086 Two-way Anova, Dunn's post test (distribution analyses: data passed normality test). *P-value*  
1087 <0.05 \*, <0.01 \*\*. Scale bars (equivalent for WT and cKO): 15  $\mu$ m at E12.5 and 30  $\mu$ m at  
1088 E15.5.

1089

1090 **Figure 4. Eml1 interacting partner analyses reveal centrosomal protein Cep170 as an**  
1091 **interactor, and reduced presence at the centrosome in *Eml1* mutant cells *in vivo*.** **A.**  
1092 BioID workflow to identify proximal interactors of EML1 and EML1\*T243A. **B.** For EML1  
1093 and EML1\*T243A BioID analysis, each hit is represented on the scatter plot displays by its  
1094 Saint Probability (SP) score versus its fold change in the spectral count over the control. **C.**  
1095 Venn diagram displaying overlapping hits for EML1 and EML1\*T243A with an  $SP \geq 0.6$ . **D.**  
1096 Heat map showing the SP scores of EML1 and EML1\*T243A proximal interactors. **E.** Gene  
1097 ontology (GO) annotation grouped into biological process of EML1 and EML1\*T243A  
1098 proximal interactors. **F.** Proximal interactors of EML1 related to microtubule cytoskeleton,  
1099 spindle, and organelle cellular components (underlined proteins lose interaction significance  
1100 in EML1\*T243A  $SP < 0.6$ ). **G.** Representative images of Cep170 labelling at the ventricular  
1101 surface in E12.5 WT and *Eml1* cKO brains **H.** Quantifications of Cep170 fluorescence  
1102 intensity at the centrosomes, also normalized to  $\gamma$ -tubulin intensity, expressed as mean +/-  
1103 SEM (the *P-value* is indicated). **I, J.** Similar analyses performed at E15.5. For BioID  
1104 experiments each condition has three replicates stemming from three independent  
1105 experiments. Cep170 fluorescence intensity analyzes were performed from at least 4  
1106 individuals per genotype from 3 different litters and 2 ROI analyzed per individual. Test and  
1107 significance: Mann-Whitney. *P-value* <0.05 \*. Scale bars (equivalent for WT and cKO): 10  
1108  $\mu$ m.

1109

1110 **Figure 5. Centrosomal alterations in human patient and mouse mutant cells.** **A.**  
1111 Representative electron microscopy (EM) images of control and EML1 patient cortical

1112 progenitors. Cells are untreated or treated with Epothilone D (EpoD). **B.** Quantifications (cells  
1113 with defective centrosomes, black arrowhead in A, and MT aggregates, circled in A)  
1114 performed on treated or non-treated human cells, values expressed as mean +/- SEM. **C.**  
1115 Representative images of pericentrin and  $\gamma$ -tubulin labelling on Pax6+ cells cultured from WT  
1116 and *Eml1* cKO embryonic brains. Enlargement of pericentrin is shown in the right panel and  
1117 the red contours show the pericentrin areas in WT and *Eml1* cKO cells. **D.** Quantification of  
1118 the total number of centrosome puncta per cell, and  $\gamma$ -tubulin fluorescence intensity per  
1119 centrosome represented as mean +/- SEM. **E.** Quantification of pericentrin fluorescence  
1120 intensity and pericentrin area represented as mean +/- SEM.  $\gamma$ -tubulin and pericentrin intensity  
1121 were analyzed in 90 WT and 89 cKO cells from 3 independent cultures, indicated by different  
1122 colors. Pericentrin area measurement was performed on 72 WT cells and 73 cKO cells. Test  
1123 and significance: Mann-Whitney. *P-value* <0.0001 \*\*\*\*\*. Scale bars: for A 0.2  $\mu$ m (equivalent  
1124 for all images); for C (equivalent for WT and cKO): 5  $\mu$ m (for main and insets).

1125

1126 **Figure 6. Eml1 is essential for the recruitment of key proteins at the centrosomes in**  
1127 **early corticogenesis. A.** Representative images of immunofluorescence labelling of  $\gamma$ -tubulin  
1128 at the ventricular surface of embryonic coronal sections at E12.5 from WT and *Eml1* cKO  
1129 individuals. **B.** Quantifications of  $\gamma$ -tubulin (+) puncta distribution from the 0 to 70  $\mu$ m from  
1130 the apical surface at E12.5 in WT and *Eml1* cKO embryonic brain sections, expressed as  
1131 mean +/- SEM. **C.** Quantification of  $\gamma$ -tubulin fluorescence intensity at E12.5 (the *P-value* is  
1132 indicated), expressed as mean +/- SEM. **D, E, F.** Similar analyses performed at E15.5. **G.**  
1133 Representative images of pericentrin labelling at the ventricular surface at E12.5 in WT and  
1134 *Eml1* cKO brains, and quantification of pericentrin dispersion at E12.5, expressed as mean +/-  
1135 SEM. **H.** Similar analyses performed at E15.5 (the *P-value* is indicated). For centrosome  
1136 analyses *n*=5 individuals from 3 litters were analyzed per genotype and age. 2 ROI were  
1137 analyzed per individual. For pericentrin area analyses: at least 4 individuals were analyzed  
1138 from 3 litters per genotype and age. Test and significance: Two-way Anova, Bonferroni post  
1139 tests (distribution analyses: data passed normality test), Mann-Whitney. *P-value* <0.05 \*.  
1140 Scale bars (equivalent for WT and cKO): 30  $\mu$ m (for A and D); 10  $\mu$ m in G, H (main), 5  $\mu$ m  
1141 (for G,H insets).

1142

1143 **Figure 7. Microtubule regrowth at centrosomes is impaired in *Eml1* mutant conditions.**  
1144 **A.** Representative images for pericentrin+ puncta ('centrosomes') with  $\alpha$ -tubulin labeling  
1145 ('MTs') on WT and *Eml1* cKO cells after ice recovery MT assays (1 and 2 minutes). **B.**  
1146 Quantifications of percentage (%) of centrosomes exhibiting MT regrowth after 1 or 2  
1147 minutes per analyzed ROI, represented as mean +/- SEM **C.** Quantifications for mean length  
1148 of MTs per centrosome 2 minutes after ice recovery, represented as mean +/- SEM ( $n=49$   
1149 centrosomes for *Eml1* cKO and 53 for WT). 16 ROI analyzed from 2 different cultures after 2  
1150 min and 12 ROI analyzed from 2 different cultures after 1 min. Different cultures are  
1151 indicated by dots of different colors. Test and significance: Mann-Whitney. *P*-value <0.01 \*\*,  
1152 <0.001 \*\*\*. Scale bars (equivalent for WT and cKO, and for 1 min, 2 min): 10  $\mu$ m.

1153

1154 **Figure 8. Abnormal detachment and subsequent heterotopia formation is partially**  
1155 **rescued with EpoD treatment.** **A.** Representative images of Pax6 labelling for WT and *Eml1*  
1156 cKO in saline or EpoD conditions at E13.5. **B.** Quantification of the cortical wall and  
1157 ventricular zone (VZ) thickness and **C.** total count for Pax6+ cells and distribution outside of  
1158 VZ in WT and *Eml1* cKO from saline and EpoD conditions represented as mean +/- SEM  
1159 ( $n=6$  individuals from 2 litters at least, indicated by dots of different colors). **D.**  
1160 Representative images of the heterotopia volume in 3D visualized by SatB2  
1161 immunofluorescence. The homotopic cortex is depicted in transparency (purple) and the  
1162 heterotopia is shown with a solid rendering (red). *Eml1* cKO embryos received saline or EpoD  
1163 at E11.5 and E12.5 and were analyzed at E18.5. Three different angles are shown. **E.**  
1164 Quantification of the ratio between heterotopia volume and that of the homotopic cortex in  
1165 *Eml1* cKO with Saline or EpoD, represented as mean +/- SD ( $n = 7$  embryos from 2 litters).  
1166 Two independent litters are color-coded. **F.** Quantification of Satb2 mean fluorescence  
1167 intensity in the homotopic cortex in *Eml1* cKO with Saline or EpoD, expressed as mean +/-  
1168 SD. Tests and significance: Two-way Anova, Sidak multiple comparison (Pax6 analyses, CW  
1169 and VZ thickness. data passed normality test), Mann Whitney test (heterotopia volume and  
1170 Satb2 analyses).  $n=7$  samples from 2 litters. *P*-value <0.05\*, <0.01 \*\*, <0.001 \*\*\*, <0.0001  
1171 \*\*\*\*. Scale bars: 50  $\mu$ m in A (equivalent for WT and cKO, all conditions) and 500  $\mu$ m in D.

1172

1173 **Supplementary Figure 1. Forebrain inactivation of *Eml1* leads to subcortical heterotopia**  
1174 **in mouse.** **A.** Schematic representation of the alleles used to generate *Eml1* cKO animals. **B.**



1175 Cresyl violet staining of individual brains at 8 weeks showing SH (red outline) in homozygote  
1176 mutant animals. **C.** Representative images of SatB2 immunofluorescence in 3D visualized by  
1177 light sheet microscopy in a control E18.5 embryo compared to an *Eml1* cKO. No heterotopia  
1178 can be detected in the control. The homotopic cortex is depicted in transparency (purple) and  
1179 the heterotopia is shown with a solid rendering (red). Three different angles are shown. **D.**  
1180 Western blot analyses showing that Eml1 expression is lost in P7 cortices. Specific anti-Eml1  
1181 antibodies 3E8 are shown in upper panels, and C3GTX in lower panels. Scale bars (equivalent  
1182 for WT and cKO): 250  $\mu\text{m}$  in B (main); 100  $\mu\text{m}$  in B inset; 500  $\mu\text{m}$  in C.

1183

1184 **Supplementary Figure 2. Altered proportion of cells in cell cycle phases in *Eml1* mutant**  
1185 **conditions.** **A.** Examples of PCNA and Ki67 labelling patterns (cropped nuclei) for different  
1186 cell cycle phases, punctate Ki67 or PCNA are indicated with a red arrow. **B.** Representative  
1187 images for PCNA and Ki67 labelling at E12.5 in WT and *Eml1* cKO cells in the VZ. **C.**  
1188 Quantification for percentage of proliferating cells in S, G1 or G2/M phases of the cell cycle  
1189 expressed as mean $\pm$  SEM.  $n=6$  individuals per genotype at E12.5. **D, E.** Similar analyses  
1190 were performed at E15.5, with  $n=5$  per individuals per genotype. Test and significance: Two-  
1191 way Anova, Sidak's multiple comparison (E12.5), Tukey's post-test at (E15.5). Data passed  
1192 normality test. *P-value* <0.05 \*, <0.001 \*\*\* Scale bar (equivalent for WT and cKO): 30  $\mu\text{m}$ .

1193

1194 **Supplementary Figure 3. BioID and gene ontology analyses of WT and T243A Eml1**  
1195 **interacting partners, Cep170 cell analyses.** **A.** Centrosomes were carefully checked in  
1196 transfected Neuro2A cells, in interphase and during mitosis. No obvious abnormalities were  
1197 identified. **B, C.** Gene ontology (GO) annotation grouped into molecular function (B) and  
1198 cellular component (C) of EML1 and EML1\*T243A proximal interactors. **D.** Representative  
1199 immunoblots of co-immunoprecipitation of EML1 and EML4. Mutant EML1 was not  
1200 assessed. **E.** Analyses of individual puncta of Cep170 fluorescence intensity at the  
1201 centrosomes, also normalized to  $\gamma$ -tubulin intensity, expressed as mean  $\pm$  SEM ( $n = 4$   
1202 embryos from 2 litters, 2 ROI analyzed per embryo). Test and significance: Mann-Whitney.  
1203 *P-value* <0.0001 \*\*\*\*. Scale bar (equivalent all images): 10  $\mu\text{m}$ .

1204

1205 **Supplementary Figure 4. Trafficking to the PC is altered in *Eml1* cKO RG. A.**  
1206 Schematized method of the Retention Using Selective Hook (RUSH) approach, used here for

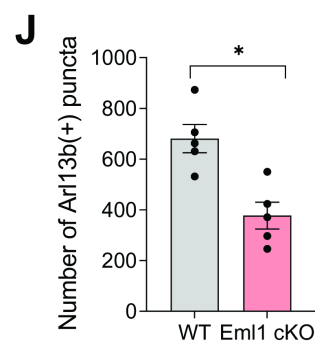
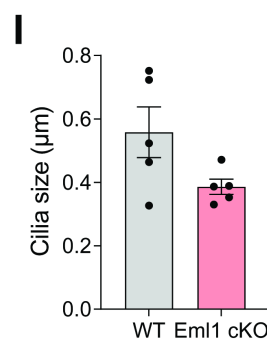
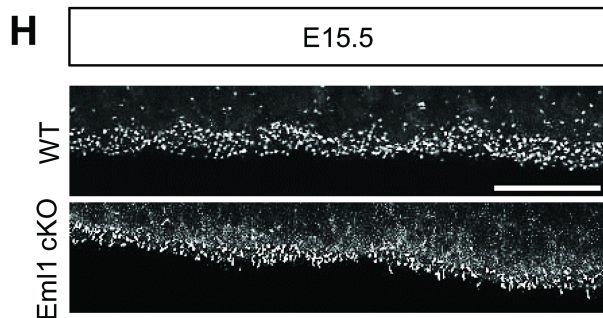
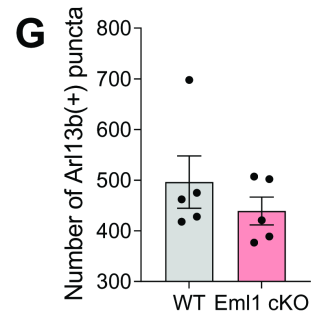
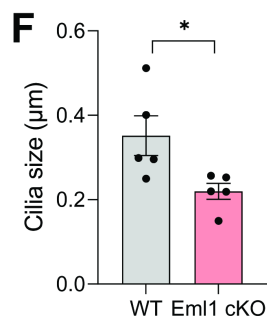
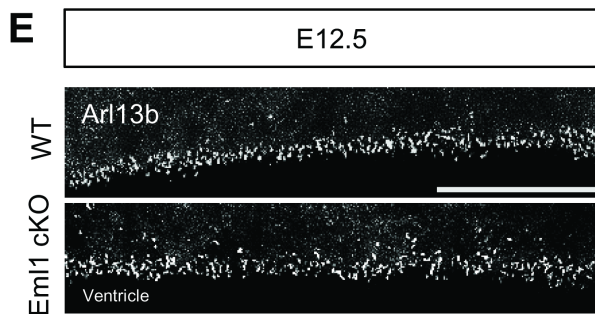
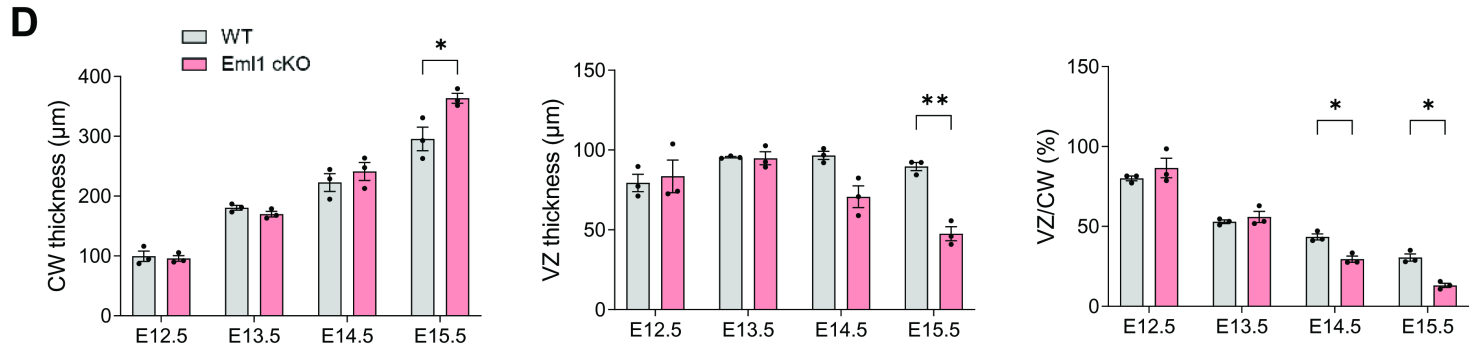
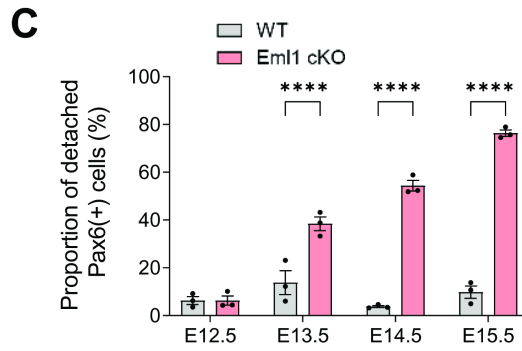
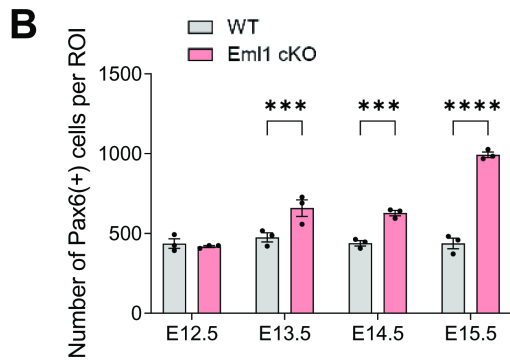
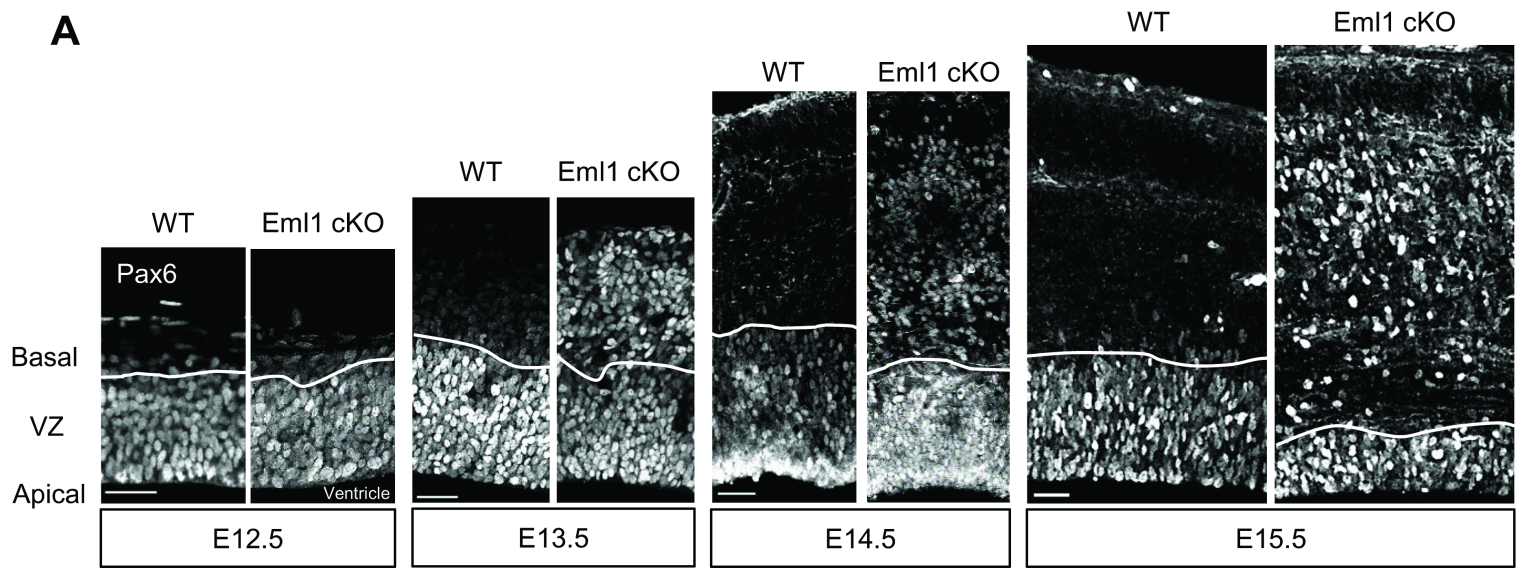
1207 PC protein trafficking analyses in primary cultures of Pax6+ cells. **B.** Representative images  
1208 of GM130, Arl13b labelling and SSTR3-GFP signal on WT and *Eml1* cKO cells in culture at  
1209 the different time points analyzed. Quantifications for SSTR3 (**C**), PKD2 (**D**) RUSH construct  
1210 concentration in the Golgi and in the PC over time (0, 30, 60 and 90 min) in WT and *Eml1*  
1211 cKO cells in culture, values represent mean +/- SEM. Quantifications were performed on at  
1212 least 15 cells from two independent cultures for each genotype and analyzed protein. Test and  
1213 significance: Two-way Anova. Sidak's multiple comparison. Data distribution was assumed  
1214 to be normal. *P-value* <0.05 \*, <0.01 \*\*, <0.001 \*\*\*. Scale bar (equivalent for WT and cKO,  
1215 all timepoints): 5  $\mu$ m.

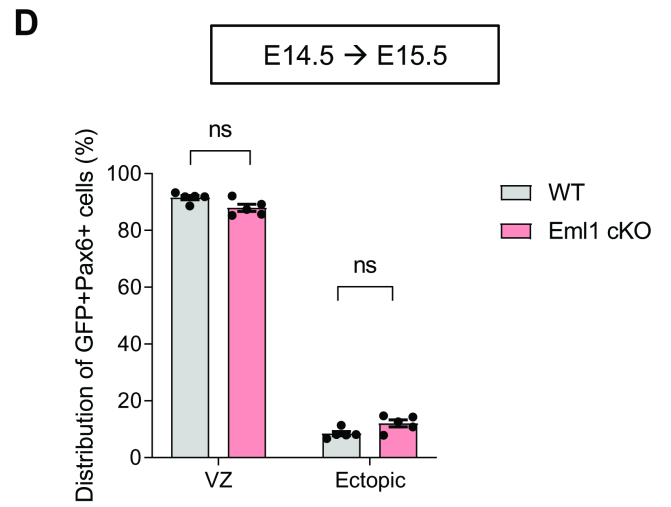
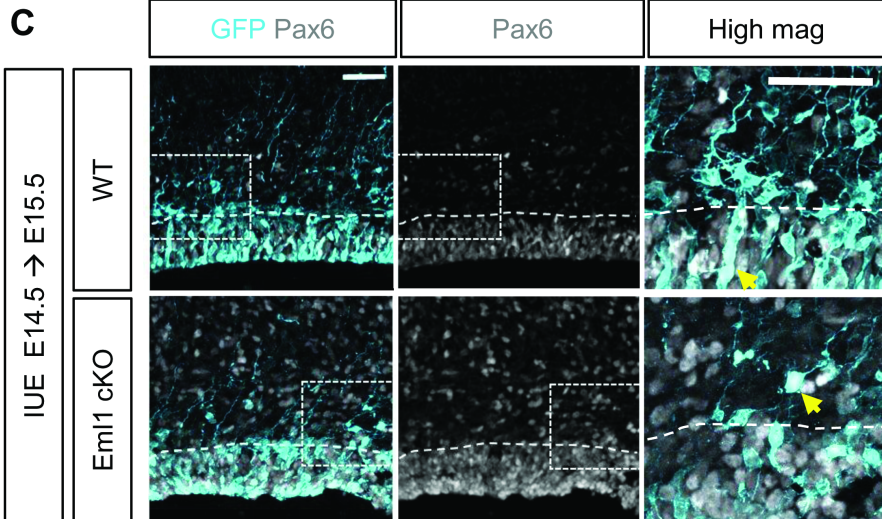
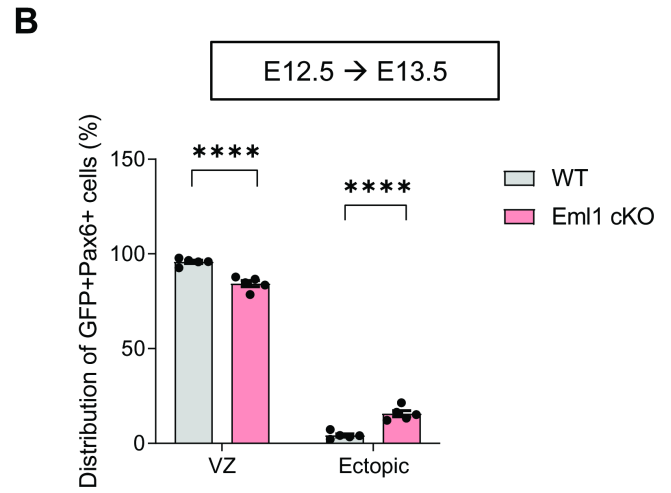
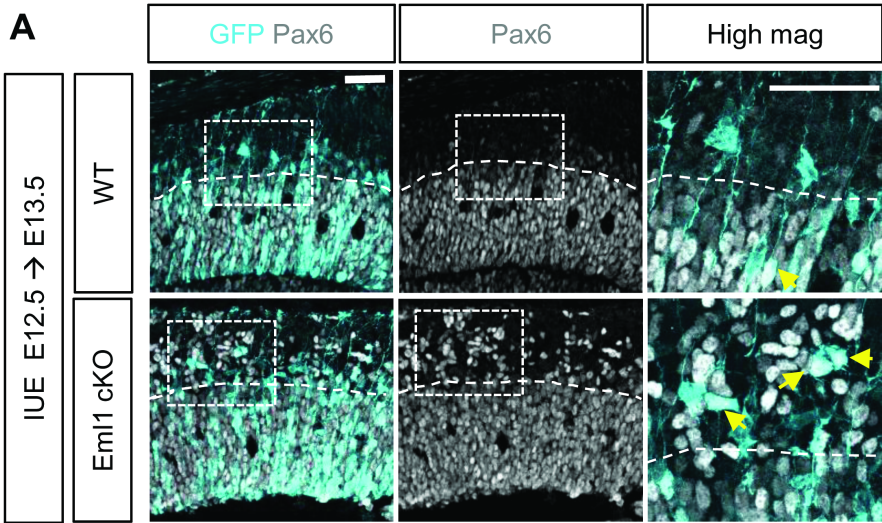
1216

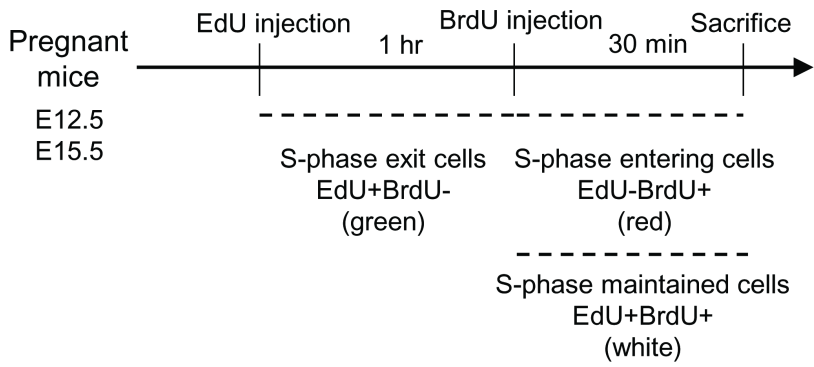
1217 **Supplementary Figure 5. Centrosome and  $\alpha$ -tubulin modifications at E12.5 and/or E15.5**  
1218 **in WT and *Eml1* cKO brains.** **A.** Analyses of overall numbers of  $\gamma$ -tubulin puncta at each  
1219 stage. **B, C.**  $\gamma$ -tubulin intensity (B) and pcnt dispersion (C) analyses at E12.5 and E15.5 by  
1220 individual puncta, expressed as mean +/- SEM. For centrosome analyses *n*=5 individuals from  
1221 3 litters were analyzed per genotype and age. 2 ROI were analyzed per individual. For  
1222 pericentrin area analyses: at least 4 individuals were analyzed from 3 litters per genotype and  
1223 age. **D.** Immunolabelling of  $\alpha$ -tubulin on embryonic brain slices at E12.5 in WT and *Eml1*  
1224 cKO. **E, F.** Quantifications from the ventricular surface to 100  $\mu$ m height show a reduction in  
1225 intensity, especially close to the ventricular surface. Quantification of  $\alpha$ -tubulin mean  
1226 intensity per ROI (47% decrease was observed in the VZ). Values represent mean +/- SEM (*n*  
1227 = 4 embryos for each case). Test and significance: Mann-Whitney ( $\gamma$ -tubulin and pcnt  
1228 analyses), Two-way Anova ( $\alpha$ -tubulin analyses, data distribution was assumed to be normal  
1229 but this was not formally tested). *P-value* <.0.001 \*\*\*, <0.0001 \*\*\*\*\*. Scale bar (equivalent  
1230 for WT and cKO): 30  $\mu$ m.

1231 **Supplemental Video 1:** 3D visualization of Satb2 staining (in green) of a cortex from a wild  
1232 type E18 embryo, with corresponding surfacing.

1233 **Supplemental Video 2:** 3D visualization of Satb2 staining of a cortex from an *Eml1* cKO  
1234 E18 embryo, with corresponding surfacing. The homotopic cortex is depicted in green  
1235 whereas the heterotopia is shown in pink.



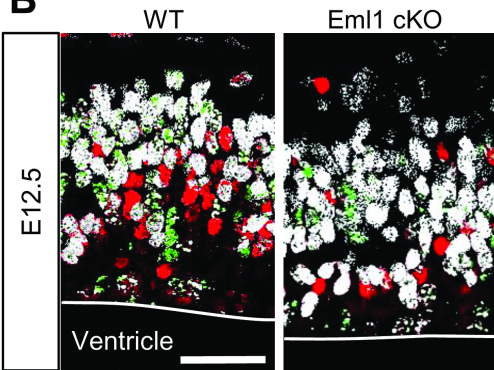
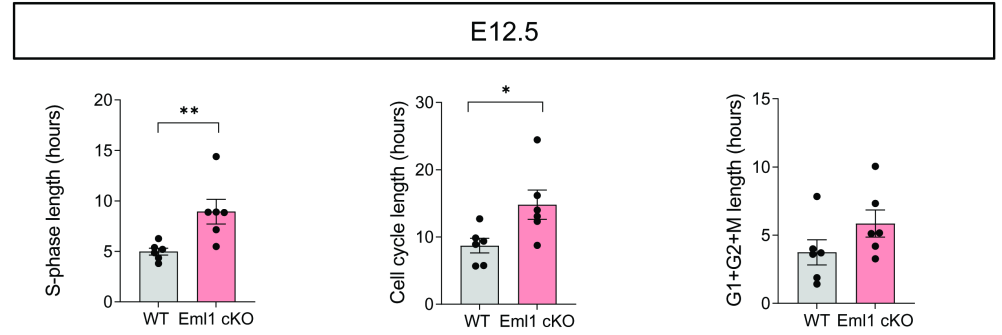
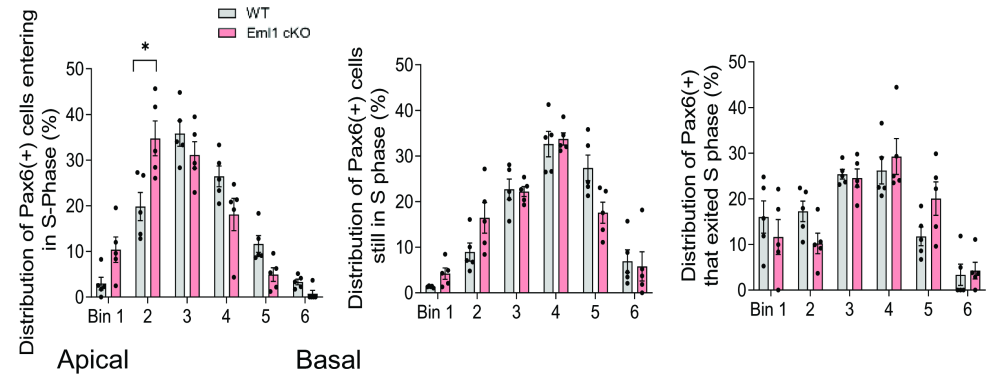
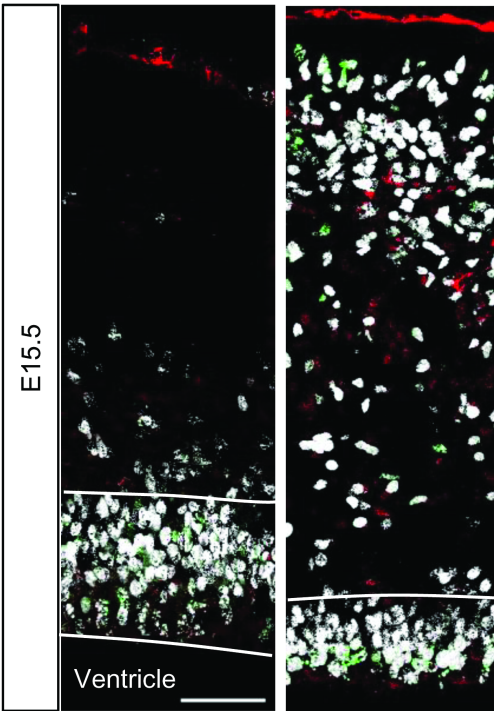
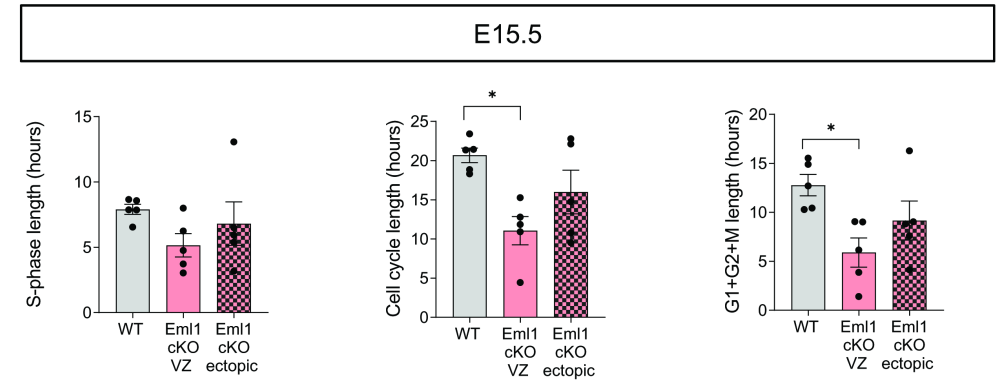
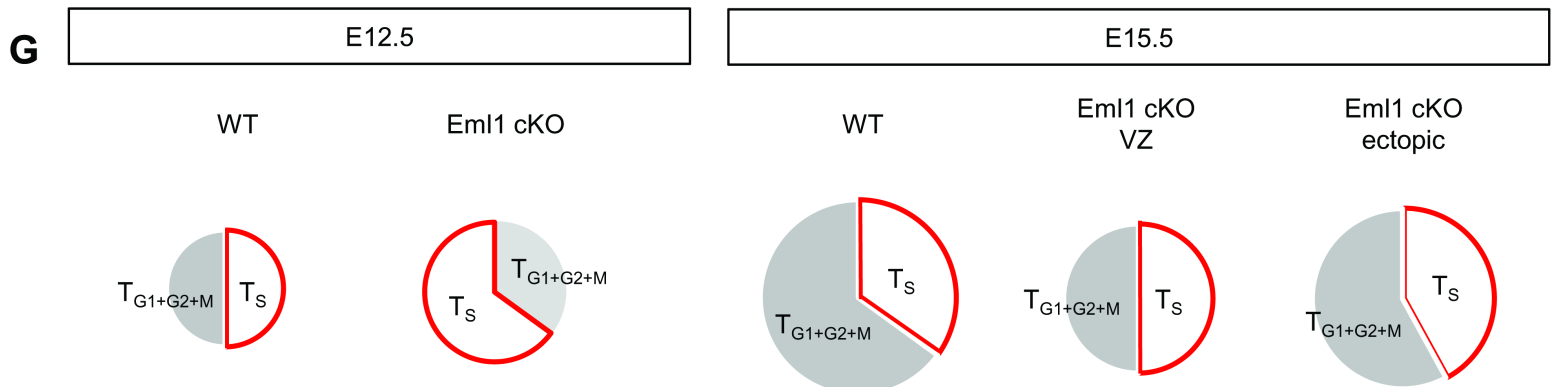


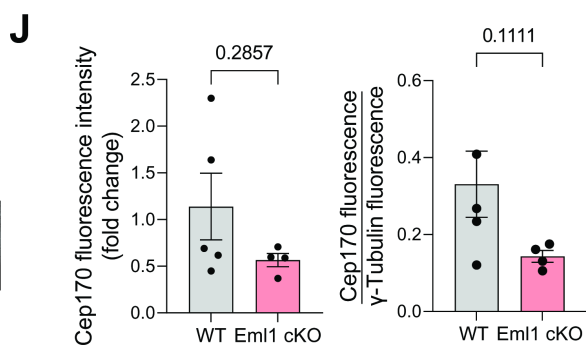
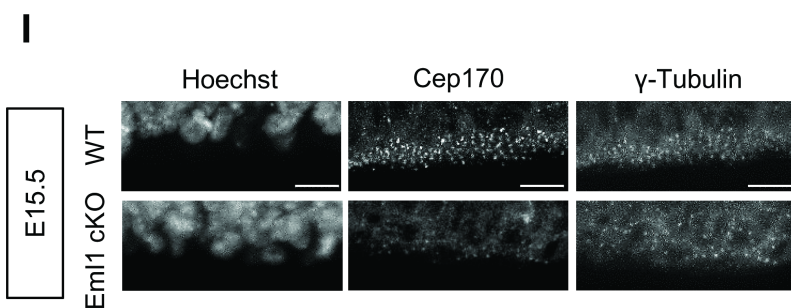
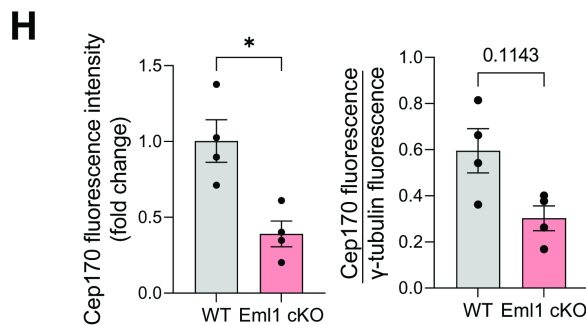
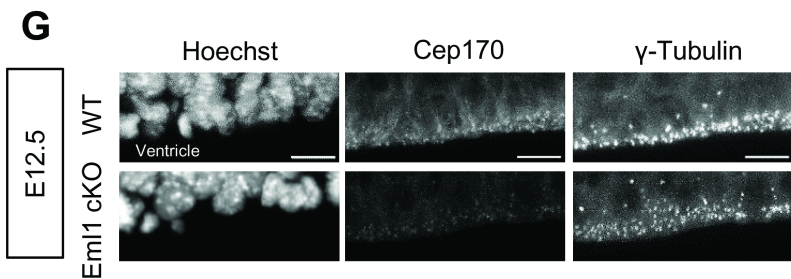
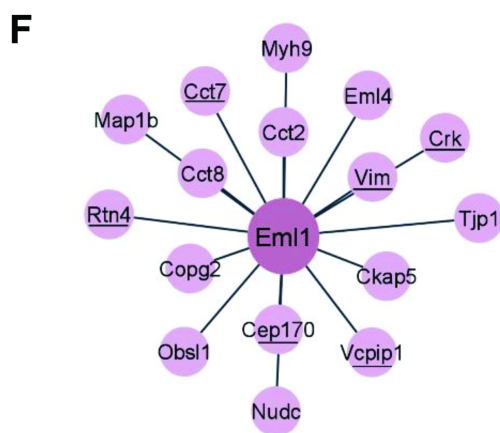
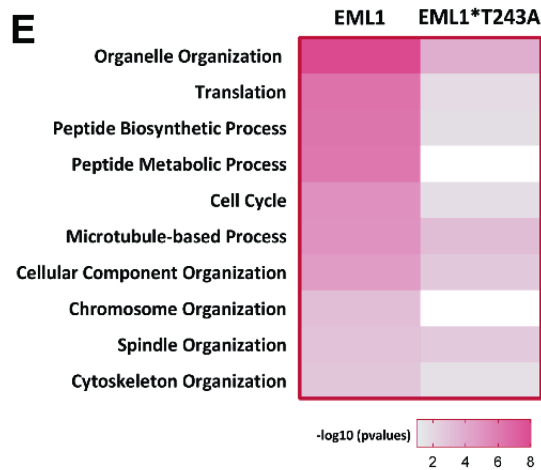
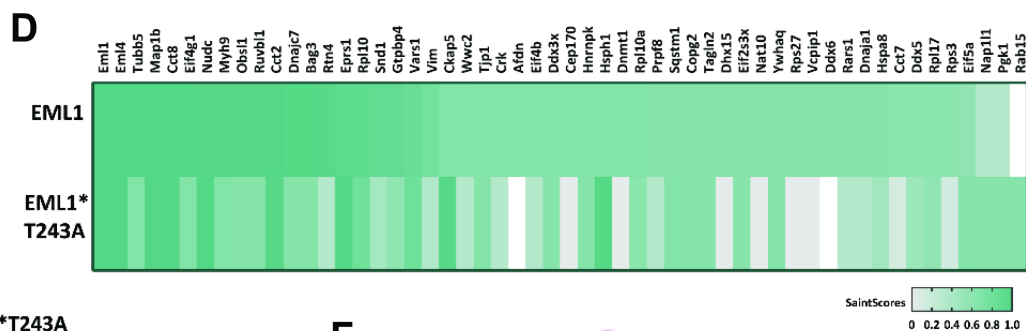
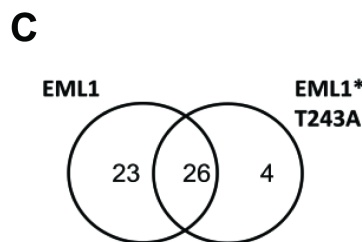
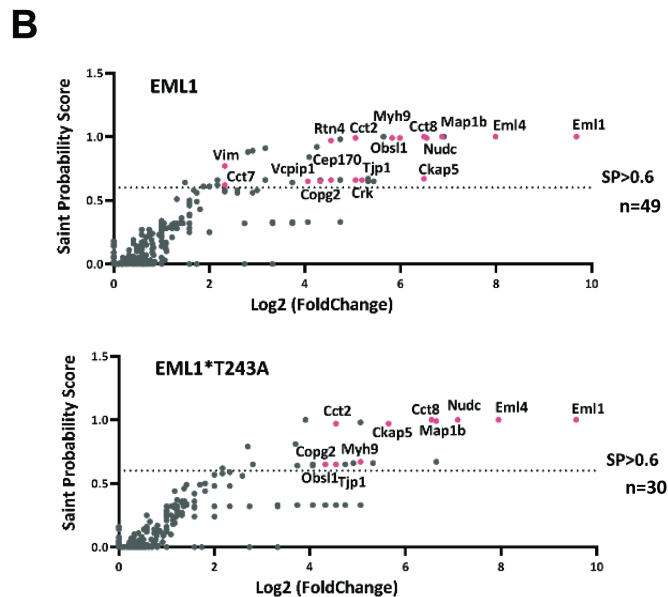
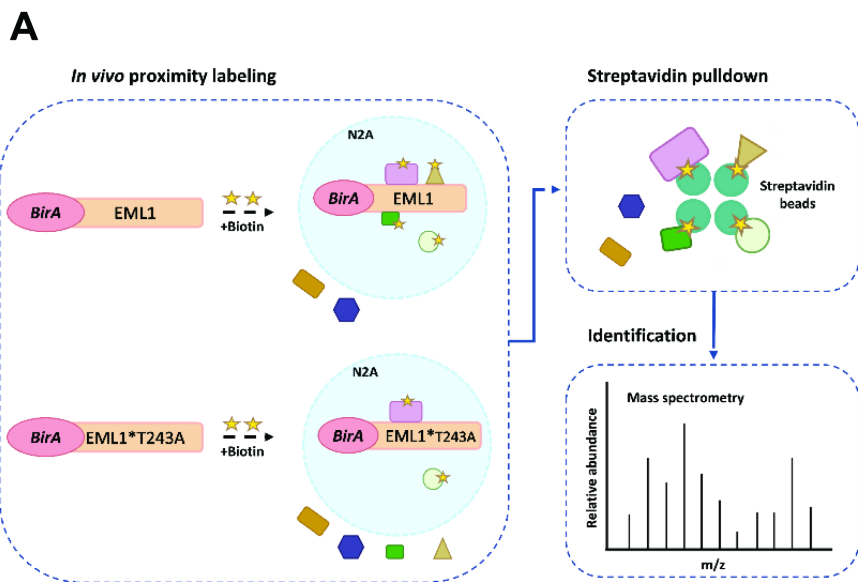
**A**

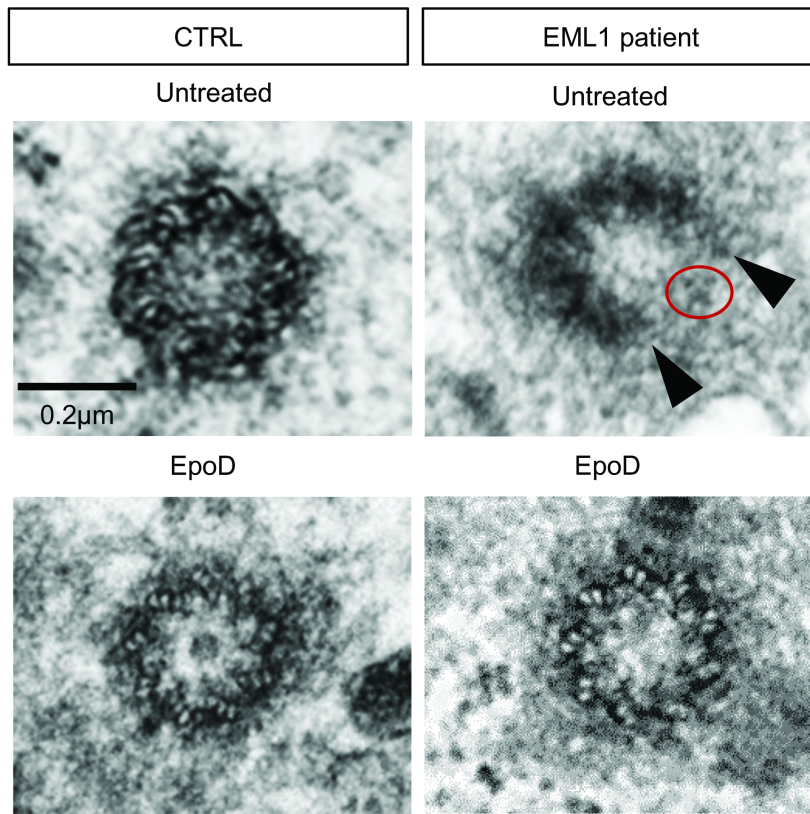
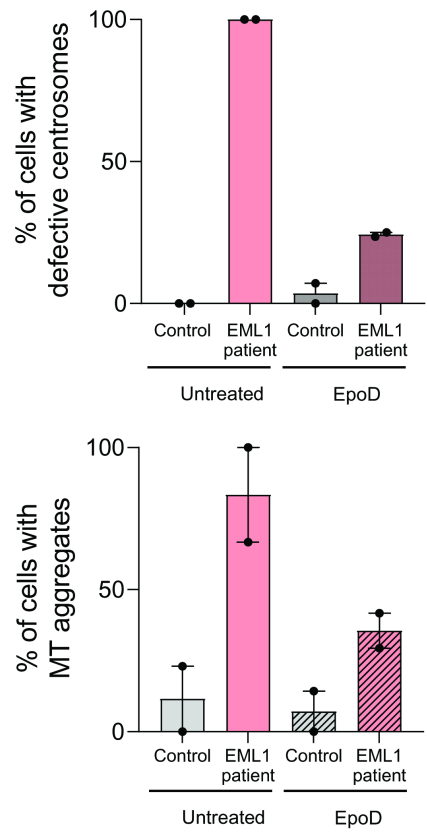
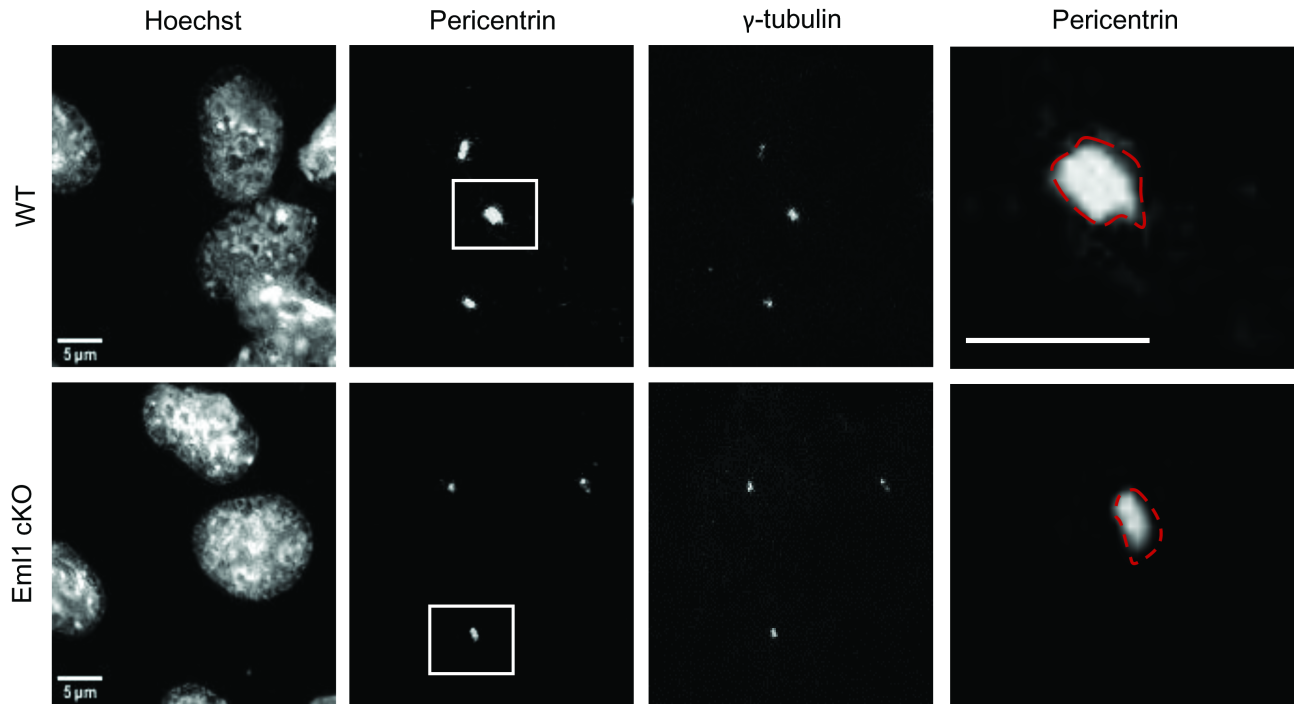
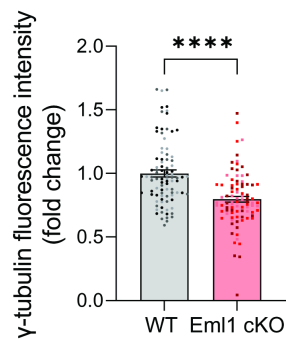
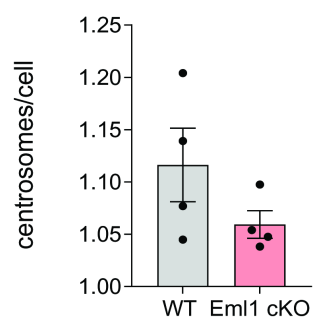
$$S\text{-phase length } (T_s) = \frac{\text{EdU+BrdU+}}{\text{Edu+Brdu-}}$$

$$\text{Cell cycle length } (T_c) = \frac{T_s}{[(\text{Edu+Brdu+})+(\text{Edu-Brdu+})]/\text{Pax6+}}$$

$$G1+G2+M \text{ length } (T_{G1+G2+M}) = T_c - T_s$$

**B****C****D****E****F****G**



**A Human****B****C Mouse****D****E**